Forming Ganymede's grooves at smaller strain: Toward a self-consistent local and global strain history for Ganymede

Michael T. Bland[1], and William B. McKinnon[1]

[1] *Department of Earth and Planetary Sciences and McDonnell Center for the Space Sciences, Washington University in St. Louis, Saint Louis, MO 63130*

50 total pages including 11 figures

Submitted to Icarus

January 3, 2014

Proposed Running Head: Forming Ganymede's grooves at smaller strain.

Corresponding Author:
Michael T. Bland
Department of Earth and Planetary Sciences
and McDonnell Center for Space Science
Washington University in St. Louis
Saint Louis, MO 63130
mbland@levee.wustl.edu
phone: (314) 935-4810
fax: (314) 935-7361

Abstract

The ubiquity of tectonic features formed in extension, and the apparent absence of ones formed in contraction, has led to the hypothesis that Ganymede has undergone global expansion in its past. Determining the magnitude of such expansion is challenging however, and extrapolation of locally or regionally inferred strains to global-scales often result in strain estimates that exceed those based on global constraints. Here we use numerical simulations of groove terrain formation to develop a strain history for Ganymede that is generally consistent at local, regional, and global scales. These simulations reproduce groove-like amplitudes, wavelengths, and average slopes at modest regional extensions (10-15%). The modest strains are more consistent with global constraints on Ganymede's expansion. Yet locally, surface strains can be much larger (30-60%), consistent with observations of highly-extended impact craters. Thus our simulations satisfy both the smallest-scale and largest-scale inferences of strain on Ganymede. The growth rate of the topography is consistent with (or exceeds) predictions of analytical models, and results from the use of a non-associated plastic rheology that naturally permits localization of brittle failure (plastic strain) into linear fault-like shear zones. These fault-like zones are organized into periodically-spaced graben-like structures with stepped, inward-dipping faults. As in previous work groove amplitudes and wavelengths depend on both the imposed heat flux and surface temperature, but because our brittle strength is depth-dependent, we find (for the parameters explored) that the growth rate of topography is initially faster for lower heat flows.

Keywords: Ganymede; Tectonics; Ices.

1 Background

1.1 Ganymede's surface strain

Ganymede's iconic "grooved terrain" consists of tens- to hundreds-of-kilometers-wide swaths of parallel, periodically spaced ridges and troughs that form a complex tectonic patchwork across the surface. Dominated at the smallest scales by apparent normal faults, and at larger scales by periodic ridges and troughs (or horst and graben, see below), the grooved terrain almost certainly formed via lithospheric extension. In contrast, features formed in contraction have not been identified. Thus, Ganymede's surface is apparently dominated by extensional strain (Pappalardo et al., 2004; Collins et al., 2010). This observation has lead to the suggestion that Ganymede has experienced a period of global expansion during either differentiation (Squyres, 1980; Mueller and McKinnon, 1988) or resonance passage (Showman et al., 1997; Bland et al., 2009). Differentiation yields the greatest areal expansion (up to ∼6% (Mueller and McKinnon, 1988)) as high-density ice deep in the satellite's core is brought up to lower pressure and converts to lower-density phases. The inferred age for the grooved terrain of 2 Ga (albeit with large uncertainty) (Zahnle et al., 2003) poses a challenge for the differentiation hypothesis unless it can be delayed until relatively late in Ganymede's history (e.g., Mueller and McKinnon, 1988). The timing problem is overcome by the resonance-passage hypothesis, which can yield up to ∼2% areal expansion of Ganymede as high-pressure phases of ice melt and transition to lower-density liquid water (Showman et al., 1997; Bland et al., 2009). However, such melting is only transient (current tidal heating in Ganymede is negligible), and it's unclear how global compression during the slow refreezing of Ganymede's ice mantle would affect its surface deformation. Furthermore, Ganymede's orbital evolution into the Laplace-resonance is far from certain (see, e.g., Peale and Lee, 2002; Malhotra, 1991; Greenberg, 1987; Yoder, 1979), and need not include passage through the paleo-resonances necessary for tidal dissipation to occur.

There are several independent constraints on Ganymede's global, regional, and local strain (see Fig. 1). McKinnon (1981) argued that the increase in Ganymede's surface area must be less than ∼2% (i.e., less than 1% increase in radius) based on the observation that Galileo Regio, a large, roughly-circular region of dark terrain, retains its intact shape. Radial expansions larger than 1% should have resulted in obvious, circumferential, extensional deformation (e.g., graben) within the Regio (Fig 1A). This observational constraint is consistent with the degree of global expansion suggested by the theoretical considerations described above.

In contrast, structural analysis of Ganymede's grooved terrain itself indicate larger regional and global strains (Collins, 2006, 2008). Collins et al. (1998) estimated strains of roughly 50% in a portion of the Uruk Sulcus region from structural reconstruction of grooved terrain swaths. More general estimates of the strain required to produce large-scale grooves suggests 25-100% extension may be typical (Collins, 2006); however, images with resolution sufficient to reconstruct pre-deformation surfaces are limited. Lower-amplitude grooves are presumed to require less strain to form (Collins, 2006). Extrapolation of these strain magnitudes to the rest of the satellite suggests that Ganymede underwent an areal increase of 6 - 20%, with a nominal value of 8% (Collins, 2008, 2009) (Fig. 1C and D). The low-end estimate may be consistent with strain magnitudes resulting from differentiation; however, these estimates are generally larger than those based on Galileo Regio, and exceed the global strains resulting from internal melting. To date these difference have not been fully reconciled.

At the smallest scales, surface strain on Ganymede can be quite large. Deformed craters on Ganymede, whose initially circular shape lends itself to strain analysis without requiring an assumption of tectonic structure, indicate that localized strains can exceed 100% (Pappalardo and Collins, 2005) (Fig. 1B). Many of these measurements were performed in craters 20-30 km in diameter with extensional zones ∼10 km wide. Despite this evidence for large local strains, the majority of Ganymede's grooves must have formed at lower extensional strain (Collins, 2008, 2009). Bubastis Sulcus near Ganymede's south pole is ∼600 km across and includes large-amplitude grooves (Fig. 2). Forming the Bubastis grooves at 100% extension of the original surface would require a 300 km increase (1.8%) in Ganymede's circumference, or a 3.6% increase in Ganymede's surface area for Bubastis Sulcus *alone*. The strain magnitude exceeds that which can be produced by melting and is nearly half that produced by global expansion. Whereas Bubastis is one of Ganymede's widest groove swaths, invoking strains of 50-100% wherever large-amplitude grooves are observed would result in cumulative global strains that well exceed current estimates. This observation alone suggests that even large-amplitude grooves must be able to form at relatively small regional strains ($\sim$10%), or that large amounts of hitherto unrecognized crustal consumption has occurred.

1.2 Salient features of the grooved terrain

Truly constraining Ganymede's strain history requires a detailed understanding of the formation of its dominant extensional tectonic feature: the grooved terrain. Nearly two-thirds of Ganymede is composed of bright terrain, much of which includes tectonic structures dubbed grooves (Patterson et al., 2010). The remaining third of the surface is heavily-cratered, lower-albedo terrain. In generic terms, the grooved terrain consists of swaths of periodically spaced ridges and troughs with amplitudes of several hundred meters (Squyres, 1981; Giese et al., 1998; and Fig 2). The salient feature of the grooved terrain is the strong periodicity of the ridges and troughs within a single groove swath. Across the satellite these wavelengths vary from 3-17 km from one groove swath to the next (Grimm and Squyres, 1985; Patel et al., 1999). At large spatial scales topographic slopes are generally low, giving the grooved terrain an undulatory character (Squyres, 1981; Giese et al., 1998), though regional variations exist (see Fig 2b). In addition to the large-scale grooves first observed in *Voyager* images, higher-resolution images from *Galileo* have revealed complex, finer-scale lineations (presumably fractures) with periodic spacings of order 1 km (Pappalardo et al., 1998; Patel et al., 1999). A detailed review of grooved terrain (and Ganymede's tectonics in general) is provided in Pappalardo et al. (2004) and Collins et al. (2010).

The general description above belies the complexity and variability of bright terrain morphologies present on Ganymede. Patterson et al. (2010) subdivided the bright terrain into three basic morphologies: grooved, subdued, and irregular. Grooved terrains, the focus of this paper, consist of lanes of large-amplitude, evenly-spaced ridges and grooves. Both groove lanes and individual grooves tend to be long and straight (or gently curved) in plan, with considerable along-strike continuity (Fig. 2). In contrast, subdued bright terrain consists of relatively smooth regions of bright terrain with no grooves or subtle, low-amplitude ridge and groove structures. Irregular bright terrain consists of a tightly interwoven patchwork of grooved and subdued terrain (Patterson et al., 2010). These classifications mirror those of Collins (2006, 2008) who subdivided grooved terrain into five categories ranging from high-relief grooves (type I) to bright smooth regions (type V). Topography data indicates that some regions of bright terrain are extremely flat, suggesting a role for cryovolcanic resurfacing during bright terrain formation (Schenk et al., 2001). However, the overall role of cryovolcanism remains unclear and we neglect it in subsequent discussions, choosing to focus on the tectonic aspects of groove formation.

Even within regions of high-relief grooves (e.g., the type I grooves of Collins (2006)) significant variation in morphology exists. Within Uruk Sulcus at least two distinct groove morphologies have been identified (Pappalardo et al., 1998, 2004). In some localities flat, plank-like grooves (dubbed "lineated grooves") are separated by narrow, sharply-bounded troughs, giving the terrain a distinctly horst-and-graben-like morphology. More commonly, grooves have a ridge-and-trough-like morphology (dubbed "parallel ridged terrain") as described above. Here we focus primarily on the parallel ridge morphology, though the results described below bear on both morphologic subtypes (see also Bland et al., 2010).

1.3 Previous models of groove formation

There is broad consensus that the grooved terrain formed in extension. The pre-*Galileo* view of groove formation posited the formation of broad grabens, which were subsequently flooded with cryovolcanic material to form bright groove lanes. A second stage of extension then formed the grooves themselves via some combination of fracturing and/or graben formation (e.g. Golombek and Allison, 1981; Allison and Clifford, 1987), possibly with subsequent viscous relaxation or mass wasting of the resulting topography (Squyres, 1982; Parmentier et al., 1982). The *ostensible* absence of evidence for cryovolcanic source vents in higher-resolution *Galileo* images (though see Schenk et al., 2001) and the identification of nascent rifts in dark terrain (Prockter et al., 2000) has lead to the post-*Galileo* view that grooved terrain forms directly from dark terrain without large-scale cryovolcanic resurfacing. In this scenario, resurfacing of dark terrain occurs by tectonism alone (Head et al., 1997; Pappalardo and Collins, 2005).

In addition to de-emphasizing cryovolcanism, the picture of grooves as graben-like structures has been replaced by one in which grooves form via periodic extensional necking of the lithosphere (although these mechanisms may, in fact, be related). The extensional necking (or extensional instability) mechanism was first proposed by Fink and Fletcher (1981). Based on a then-unpublished model for the formation of the Basin and Range (Fletcher and Hallet, 1983), the mechanism proposes that the strong viscosity contrast between Ganymede's lithosphere and warmer ice at depth causes the extending lithosphere to deform into periodically spaced pinches and swells (i.e., ridges and grooves). The physical model is analogous to the formation of boudinage at outcrop scales (e.g. Smith, 1975, 1977). The idea was briefly revisited by (Golombek and Banerdt, 1986) but not rigorously evaluated until Herrick and Stevenson (1990) actually applied the Fletcher and Hallet (1983) model to icy satellites and found that Ganymede's surface was too warm to permit sufficient instability growth. In effect, the viscosity contrast between the lithospheric ice and underlying ductile ice, which controls the amplification rate of the initial topography, was thought too small to produce groove-like amplitudes (several hundred meters) for reasonable strains.

The extensional instability mechanism was rekindled in the wake of observations of small-scale, plausibly tilt-block faulting accommodating larger "*Voyager*-scale" grooves (Collins et al., 1998; Pappalardo et al., 1998). Even before the new observations, Dombard and McKinnon (1996, 2001) had revisited the Fletcher and Hallet (1983) model with the addition of the newly-discovered grain-boundary-sliding rheological mechanism for ice I (Goldsby and Kohlstedt, 1997, 2001) and the inference of colder surface temperatures at the time of groove formation (due to a faint younger Sun and possibly a higher surface albedo) and showed that instability growth rates *were*, in fact, consistent with Ganymede's grooves if

$\sim$10% extension was assumed. With the theoretical work of Dombard and McKinnon (2001) reinforcing the structural interpretation of Collins et al. (1998) and Pappalardo et al. (1998), groove formation via extensional necking instability became (and remains) the defacto driving mechanism for the development of Ganymede's iconic terrain.

In order to investigate the formation of grooved terrain in more detail, Bland and Showman (2007) performed finite element simulations of the extension of an ice lithosphere. Their models advanced beyond previous infinitesimal-strain models by permitting the investigation of groove formation at arbitrarily large extensional strains. The simulations demonstrated that lithospheric extension modified small-scale, random initial topography into strongly periodic deformation, but struggled to produce topographic amplitudes consistent with *Voyager* and *Galileo* observations. Maximum amplitudes in these simulations reached just 70 m after 30% extension. Additionally, amplitude growth rates decreased with increasing extension, effectively preventing the production of large-amplitude grooves even at very large strains. To address the lack of amplification, Bland et al. (2010) followed an approach common in the terrestrial literature and included strain weakening — in which the material strength of the ice degrades with increasing plastic (i.e., brittle) failure (Buck and Poliakov, 1998; Buck et al., 2003; Beaumont et al., 1996; Huismans and Beaumont, 2002; Delescluse et al., 2008; Gerbault et al., 2003; Gessner et al., 2007, and many others) — in new simulations of lithospheric extension. Models including weakening yielded topographic amplitudes as large as 230 m after 20% strain and 500 m after 30% strain (but note that the highest-strain simulations in Bland et al. (2010) were affected by substantial plastic dilation, see below). Whereas the amplitudes produced are more consistent with Ganymede's actual grooves, the strain necessary to produce the morphology (20-30%) is still a factor of several larger than those inferred from conservative estimates of Ganymede's global strain.

1.4 Current Objectives

Here we present new finite element simulations of lithospheric extension that produce topographic deformation (e.g., amplitude and periodicity) consistent with Ganymede's grooves after just 10–15% total extension. The larger amplitude-growth rates, which are similar to rates inferred by infinitesimal strain calculations (Dombard and McKinnon, 2001), result not from material weakening (as in Bland et al. (2010)) but from a more realistic formulation of continuum brittle deformation than used in previous models (e.g., Bland and Showman, 2007): so-called non-associative plasticity. These simulations provide the first finite strain calculations consistent both with groove morphology and the global strain history of Ganymede.

2 Methodology

We use the finite element code Tekton2.3 (originally written by Melosh and Raefsky (1980)) to simulate the extension of an ice lithosphere and underlying ductile ice. Both the model and the basic approach have been described in detail elsewhere (e.g., Bland and Showman, 2007; Bland et al., 2010), and only the most salient details are provided here.

We use a rectangular finite element domain nominally 80 km long and 24 km deep. The domain is long enough to accommodate the formation of long wavelength topography and deep enough to insure negligible influence from the bottom boundary. The mesh resolution is 166 m by 250 m in the horizontal and vertical directions, respectively: small enough to resolve both short-wavelength deformation and high thermal gradients. Lower heat flux simulations used longer and deeper domains (e.g., 160×40 km for the 25 mW m^{-2} and 50 mW m^{-2} simulations). Extension is imposed with a fixed horizontal displacement condition on the left boundary and a constant horizontal velocity condition on the right boundary. Free slip conditions are imposed in the vertical direction on the left and right boundary, and in the horizontal direction on the bottom boundary. The bottom boundary is fixed in the vertical direction and the top of the domain is a free surface. Initial topography is introduced by seeding the top surface of the domain with a low-amplitude (15 m maximum), random topographic perturbation consisting of 80 randomly phase-shifted and co-added sinusoids. The domain is initialized with gravitational stresses appropriate for Ganymede

($g = 1.44$ m s^{-2}).

As discussed above, (Section 1) we suggest that even large-amplitude grooves must form at extensional strains of ~10%, consistent with estimates of Dombard and McKinnon (2001). We thus nominally impose 10% extensional in our simulations, though in a few cases we investigate larger strain. We use a nominal strain rate of 10^{-13} s^{-1} corresponding to 10% strain in 3×10^4 years and investigate a limited number of cases with strain rates of 10^{-14} s^{-1} (10% strain in 3×10^5 years). Investigation of even lower strain rates require prohibitively long computation times (unless we, for example, lower the spatial resolution). The time scales involved in groove formation are largely unconstrained, though recent simulations of mobile-lid convection (a plausible driver for Ganymede's surface strain) suggest strain rates of 10^{-13} to 10^{-14} (Hammond and Barr, 2013), consistent with the values used here.

Tekton does not include thermodynamics, but we impose a static heat flux via a predefined viscosity structure. We investigate heat fluxes of 25 mW m^{-2} to 150 mW m^{-2}. These heat fluxes exceed the expected radiogenic heat flux at the time of groove formation, but are consistent with heat fluxes due to passage through a Laplace-like paleo-resonance (Bland et al., 2009; Showman et al., 1997) and/or mobile-lid convection (Hammond and Barr, 2013). Lower heat fluxes fail to produce groove-like deformation (Dombard and McKinnon, 2001; Bland and Showman, 2007; Bland et al., 2010). Our nominal simulations use a cold surface temperature of 70 K, consistent with polar temperatures at the time of groove formation (brighter terrain, and a faint younger Sun). These temperatures are quite cold, and were intentionally chosen to produce the maximum plausible groove topography for a given strain. These simulations therefore constrain the *minimum* strain required to produce groove-like topography on Ganymede. Additionally, the low temperature permits direct comparison to our previous models that used T_s=70 K. The effect of surface temperature on groove development is discussed in detail in Section 3.5. For numerical efficiency we limit the maximum temperature at depth to 220 K (the low viscosities associated with high temperatures require increasingly small time steps to resolve the Maxwell time). This temperature limit slightly inhibits amplitude growth relative to a "real" ice shell where T_{max} is near 250-260 K for a convective ice shell; however, our basic results are unaffected. The surface temperature and heat flux define the complete temperature structure through the lithosphere assuming the thermal conductivity is known. The thermal conductivity, k, of pure, solid ice is temperature dependent with the form $k = 651\,\mathrm{W\,m^{-1}}/\mathrm{T}$, where T is the temperature (Petrenko and Whitworth, 1999). The viscosity structure is calculated from the temperature structure.

The model is viscoelastic-plastic in two dimensional plane strain. The total strain rate is thus given by the sum of the elastic, viscous, and plastic strain rates,

$$\dot{\varepsilon}_{total} = \dot{\varepsilon}_e + \dot{\varepsilon}_v + \dot{\varepsilon}_p. \tag{1}$$

We assume a Young's modulus of 9.33 GPa and a Poisson's ratio of 0.325, consistent with intact ice (Gammon et al., 1983). Decreasing the Young's modulus (e.g., due to the presence of near-surface fractures) generally suppresses amplification rates (Bland and Showman, 2007), but said fractures would produce a compensated effect by increasing the thermal gradient. The model incorporates the known (measured) viscous deformation mechanisms for ice I (dislocation creep regimes 'A,' 'B,' and 'C,' grain-boundary-sliding, and basal slip) using a composite rheology of the form (Durham and Stern, 2001)

$$\dot{\varepsilon}_v = \dot{\varepsilon}_A + \dot{\varepsilon}_B + \dot{\varepsilon}_C + \left[(1/\dot{\varepsilon}_{GBS}) + (1/\dot{\varepsilon}_{BS})\right]^{-1}. \tag{2}$$

where each $\dot{\varepsilon}$ refers to the strain rate for each rheological mechanism as denoted by the subscripts A, B, C, GBS, and BS, and $\dot{\varepsilon}_v$ is the total viscous strain rate.

The rheological law and parameters used in our simulations are standard and given in Bland et al. (2010). The GBS deformation mechanism is grain-size sensitive. Grain sizes in the interiors of icy satellites are unconstrained by direct observations. We assume a grain size of 1 mm as in our previous work (see Barr and McKinnon (2007) and Bland and McKinnon (2012) for a discussion of the limited constraints on grain size in icy satellites).

Plasticity is a continuum approach to modeling brittle failure that requires defining both a yield criterion (i.e., a stress threshold at which material fails brittlely) and a plastic flow law (i.e., a constitutive relation defining $\dot{\varepsilon}_p$). We use a Drucker-Prager yield criterion with the form (Owen and Hinton, 1980; Vermeer and de Borst, 1984; Iwashita and Oda, 1999)

$$J_2^{\frac{1}{2}} = \beta - \alpha I_1, \tag{3}$$

with a corresponding plastic potential of

$$F(\boldsymbol{\sigma}) = J_2^{\frac{1}{2}} + \alpha I_1 - \beta. \tag{4}$$

Drucker-Prager is analogous to a Mohr-Coloumb criterion, but varies smoothly in stress-space; I_1 is the first invariant of the stress tensor $\boldsymbol{\sigma}$ (i.e., the trace, with stress negative in compression), and β and α are related to the more familiar cohesion (c) and angle of internal friction (ϕ) by

$$\beta = \frac{6c\cos\phi}{\sqrt{3}(3-\sin\phi)}, \qquad \alpha = \frac{2\sin\phi}{\sqrt{3}(3-\sin\phi)}. \tag{5}$$

Plastic failure occurs when the square root of the second invariant of the deviatoric stress J_2 reaches or exceeds the yield criterion in Eq. 3. Upon element failure, the stresses are returned to the yield surface defined by Eq. 3 via plastic flow ($\dot{\varepsilon}_p$). Two related approaches can be used to model plastic flow. In associated plasticity, the plastic flow law is a function of the gradient of the plastic potential F in stress space, and thus by definition is directed perpendicular to the yield surface (i.e., $\dot{\varepsilon}_{plast} \propto \frac{\partial F}{\partial \boldsymbol{\sigma}}$). While straightforward to implement numerically, the formulation results in substantial element dilation when used with a failure criterion that depends on the mean stress. That is, the volumetric plastic strain is always positive (Davis and Selvadurai, 2005). While geologic materials are known to dilate (bulk) on failure (clays being an exception), the magnitude of dilation resulting from associated plasticity is typically larger than that actual observed experimentally. When accumulated over many cycles of failure, the dilation can substantially (and unrealistically) distort the finite element mesh in high strain regions.

The alternative to associated flow (or its generalization) is a non-associated flow law that defines $\dot{\varepsilon}_p$ as a function of a more general plastic potential g (i.e., $\dot{\varepsilon}_p \propto \frac{\partial g}{\partial \boldsymbol{\sigma}}$). A plastic potential that limits element dilation can then be constructed. It is well established that granular geologic materials undergo limited dilation during shear failure (Vermeer and de

Borst, 1984), and fracturing ice is no exception (Lade, 2002; Pritchard, 1988). We therefore use a non-associated flow law and define a plastic potential with the form

$$g(\boldsymbol{\sigma}) = J_2^{\frac{1}{2}} + \bar{\alpha} I_1 - \bar{\beta}, \tag{6}$$

where

$$\bar{\alpha} = \frac{2 \sin \psi}{\sqrt{3}(3 - \sin \psi)}, \qquad \bar{\beta} = \frac{6 \cos \psi}{\sqrt{3}(3 - \sin \psi)}, \tag{7}$$

where ψ is the dilation angle, an experimentally constrained parameter. The non-associated plastic flow reverts to associated flow when $\psi = \phi$. We have confirmed that our simulations using non-associated plasticity and $\psi = 30°$ are identical to our previous ones using associated plasticity when both assume ϕ=30°.

Assigning a small dilation angle permits stresses to return to the yield surface via a non-perpendicular path and effectively limits element dilation (see Davis and Selvadurai, 2005, for a clear discussion). Despite extensive study of the friction and failure properties of ice (see e.g., Schulson and Duval, 2009, and references therein), fewer direct laboratory measurements of the dilation angle of ice have been made. Studies of sea ice mechanics that include the effect of dilation have adopted dilation angles of 10° (Tremblay and Mysak, 1997; Wilchinsky and Feltham, 2011), consistent with measured dilation angles for soils, rocks, and concrete (Vermeer and de Borst, 1984). Yasufuku et al. (2008) measured dilation angles of ice-sand mixtures in a shear box and found values ranging from 5° to 18°, with ice rich samples generally having lower angles. Unless otherwise noted, we use a dilation angle of 4°, reasonably consistent with the ice-rich measurements of Yasufuku et al. (2008) and typical geologic materials undergoing extended strain in which dilation is naturally limited (i.e., $\psi \to 0$ at large strain) (Vermeer and de Borst, 1984)[1]. In addition we assume ϕ=30° and c=3 MPa for all the calculations presented here.

Not only does non-associative plasticity correctly account for the observed dilation of geologic materials, but its inclusion can also lead to localization of strain into discrete shear

---

[1] Experiments on faulted rocks and concrete actually show larger initial dilation angles, but these decrease with plastic strain as bulking is naturally limited. One way to appreciate the dilation angle is to note that in simple shear the ratio of the volumetric and shear strain is simply $\tan \psi$ (Vermeer and de Borst, 1984).

bands (Rudnicki and Rice, 1975; Vermeer and de Borst, 1984). Because non-associative plasticity naturally leads to strain localization, numerous authors have utilized it to simulate the formation of plastic shear bands in rocks (e.g., Poliakov and Herrmann, 1994). It is important to note that the localization that results from non-associated plasticity is due to a rheological instability, and is distinct from previous models that included material weakening (e.g., a decrease in cohesion and/or internal friction after yielding occurs).

3 Results

3.1 Basic results

The results of our nominal simulation with a heat flux of 100 mW m^{-2}, a strain rate of 10^{-13} s^{-1}, a surface temperature of 70 K, and an extension of 10% are shown in Fig. 3A. The surface of the domain, which was initially seeded with low-amplitude random topography, has been deformed into strongly-periodic ridges and troughs with a dominant wavelength (i.e., the average distance between adjacent peaks/troughs measured from our simulation after 10% extensions) of 7.4 km. Maximum and average peak-to-trough topographic amplitudes are 450 m and 260 m, respectively, and maximum and average slopes (calculated over 4 nodes, i.e., 500 to 600 m) are 15° and 4°, respectively. Groove amplitudes are more than an order of magnitude greater than previous models at the same extension (Bland and Showman, 2007), and *initial* amplitude growth rates ($q = \frac{\ln(A/A_\circ)}{\varepsilon} + 1$, where $A_\circ$ is the initial amplitude, and A is the amplitude after a strain of ε) are comparable to those derived from semi-analytical, infinitesimal strain models (Dombard and McKinnon, 2001) (see below). Averaged growth rates after 10% extension are a factor of 3× lower, however. We emphasize that the simulations in Fig. 3 do not utilize explicit strain localization (i.e., a decrease in yield strength with increasing strain). Despite this, groove amplitudes are a factor of four greater in the current simulations than in previous numerical models that assumed strain localization and associated plasticity (Bland et al., 2010).

Increasing the surface temperature to 100 K results in lower groove amplitude growth rates, requiring larger strain to produce similar groove morphology. The surface deformation and distribution of plastic strain for a simulation with T_s=100 K and a heat flux of 75 mW m^{-2} are shown in Fig. 3B after 14% extension. The maximum and average topographic amplitudes are 400 m and 270 m, respectively, similar to those of the T_s=70 K case. However, at 10% extension the maximum groove amplitude is only 210 m, a factor of two lower than in the simulation with T_s=70 K. Section 3.5 provides a more complete description of the effect of surface temperature on our results.

The larger groove amplitudes result from natural localization of brittle failure (i.e., plastic strain, see discussion in Section 2) within periodically-spaced, linear zones that form v-shaped (i.e., antithetically dipping) graben-like structures. Each graben-like zone corresponds to a single trough in the topography. The linear plastic strain zones are conceptually consistent with fault zones, in which brittle failure primarily occurs along a single plane, and thus serve as proxies for faults. Although the plastic zones we show have finite width (generally a single 166 m element), previous studies (including our own) indicated that such zones typically occur at the resolution limit, and that increasing the mesh resolution simply decreases the width of the fault zone without significantly changing the model behavior (Poliakov and Herrmann, 1994). We therefore predict that the plastic zone will generally localize at the scale of the mesh resolution, as would be expected for a single fault or narrow shear zone.

The fault-like zones dip at an angle of ∼55° to 60°, consistent with normal faults forming in material with an angle of internal friction of 30° (see also Fig. 9). We note that the antithetically dipping faults appear to intersect close to the brittle-ductile transition (defined as the depth at which plastic failure no longer occurs in the simulation). However, the distribution of fault-like zones within a single graben-like structure is complex. The graben-like structures are not simply bounded by two antithetic faults but a series of fault-like structures broadly distributed over regions a kilometer or more wide. Whereas the widely separated bounding faults intersect at the brittle ductile transition, interior faults intersect at shallower depths. The breadth of these boundary zones and multiplicity of fault-like structures results from the fact that, while failure is localized, the faults themselves do not weaken. Overall, the extensional deformation illustrated in Fig. 3 is broadly distributed, so that the surface topography is remarkably sinusoidal.

Lithospheric extension results in the rapid development of linear plastic zones at relatively low strains. Figure 4 shows the same simulation as in Fig. 3A but after just 1% extension. Virtually all of the strain has been accommodated on the discrete, fault-like zones, resulting in peak to trough topographic amplitudes of nearly 40 m. The amplitude growth at these small strains ($A/A_\circ = 2.86$) is actually greater than growth rates calculated from semi-analytical models of extensional necking, in this circumstance. Under the same strain rate, surface temperature, and thermal gradient conditions, Dombard and McKinnon (2001) calculated an exponential growth rate of $q \approx 50$, corresponding to amplitude growth of $A/A_\circ = 1.6$; however, the amplitudes produced by our simulations result from a more involved physical mechanism (i.e., shear localization is clearly important in our simulations). Also notable in Fig. 4 is the rapidity with which strongly periodic deformation is established from the random initial topography. The rapid establishment of a dominant wavelength is typical of our simulations generally, independent of, e.g., the prescribed heat flux (see also Fig. 6).

Fig 5A shows the amplitude of the groove topography (peak to adjacent trough) as a function of extensional strain. For clarity, the inset expands the strain interval below 1%. Topographic amplitudes initially decrease until 0.1% extension, before increasing roughly exponentially. The initial decrease in topographic amplitude likely results from the initial nucleation phase in which the topography flattens due to the extension of the layer, but before sufficient amplification of the topography can counteract it (cf. Schmalholz and Podladchikov, 2001). Once amplification of the surface topography begins, the variability in the growth curve at these small strains results from morphological changes in the surface topography as the dominant wavelength continues to establish itself. Notably, simulations using a single wavelength (i.e., the dominant wavelength) as the initial perturbation do not undergo an initial decrease in amplitude, and generally have smoother amplitude growth between 0% and 1% extension, consistent with the above interpretation.

As strain increases beyond 1%, amplitude growth remains exponential (note log scale on y-axis), but occurs at a lower rate (in what Schmalholz (2006) would term the amplification phase). In contrast to previous simulations, we do not show a transition to a kinematic phase of extension, in which growth rates decrease and are limited by the thickness of the lithosphere; however, such transitions are observed in earlier simulations (Bland and Showman, 2007), and occurred at extensional strains larger than those investigated here (i.e., >10%).

3.2 The effect of heat flux

The relationship between amplitude growth and heat flux departs from, and is more complex than, that predicted by semi-analytical infinitesimal strain models of unstable extension and our previous modeling. Figure 5B shows the maximum peak-to-trough amplitude as a function of strain for simulations with heat fluxes ranging from 25 mW m^{-2} to 150 mW m^{-2}. At low strains (e.g., $\leq$1%) our simulations indicate that initial amplitude growth is favored by *low* heat fluxes. This contrasts with our expectations form theoretical considerations of instability growth during contraction (folding) or extension (necking). Amplitude growth depends primarily on the strength contrast between the deforming layer and the surrounding matrix (e.g., Biot, 1961). High heat fluxes nominally yield the greatest contrast in strength between the lithosphere and the underlying warm ice (in that, the e-folding depth of the viscosity is smaller for high heat flows) and are therefore expected to yield the largest growth rates. This expected dependence on thermal gradient has been specifically demonstrated for ice lithospheres both analytically (Herrick and Stevenson, 1990; Dombard and McKinnon, 2001, 2006) and numerically (Bland and Showman, 2007).

In our simulations, the layer strength contrast is also influenced by the maximum stresses supported in the lithosphere. When heat flux is low, the cold lithosphere in our simulations supports large stresses (up to 10 MPa for F=25 mW m^{-2}); when the heat flux is high the lithosphere supports only lower stresses (4.5 MPa for F=100 mW m^{-2}). The factor of two difference in maximum stress has a direct effect on the strength contrast between the lithosphere and underlying ice and counters the effect of decreased e-folding depth at high heat fluxes. The *effective* strength contrast is therefore actually marginally greater for low heat flux simulations, which have larger e-folding depths but a larger total variation in strength. This effect was verified by artificially capping the maximum lithospheric stresses in our low-heat-flux simulations, thus removing the influence of lithospheric strength differences. In these cases only the e-folding depth plays a role and we see that amplitude growth is in fact favored by high heat fluxes, as previously expected.

Notably, the same effect was observed in our simulations of lithospheric folding in which the fold amplitude was effectively independent of heat flux unless we forced all of the simulations to have the same maximum lithospheric stress (Bland and McKinnon, 2012). Additionally, Bland et al. (2010), who used mechanical weakening rather non-associated plasticity to localize strain, found a similar relationship between heat flux and groove amplitude (see their Fig. 8): at large strains higher thermal gradients corresponded to lower groove amplitudes. They attributed this effect to an earlier transition to lithosphere-thickness-limited growth at high thermal gradients relative to lower thermal gradients. The early transition limits the maximum amplitudes produced by high thermal gradient simulations, permitting lower thermal gradients to yield greater total amplitude at large strain (see detailed discussion in Bland and Showman, 2007). However, Bland et al. (2010) did not examine the relationship between thermal gradient and amplitude growth at low strain, and it's plausible that low thermal gradients resulted in large deformation amplitudes even at low strains, as observed in the present work.

In addition to the effect of layer strength contrast, these models suggests that amplitude growth also depends on the strain localization resulting from the use of non-associated plasticity. Simulations with thicker lithospheres (low heat fluxes) result in longer wavelength deformation, and plastic strain is localized in fewer fault-like zones on an absolute scale (the localization per wavelength is unchanged). This results in higher absolute strain and larger topographic growth in each zone (the growth in normalized topography, A/λ, is lesser by comparison). In contrast, when the lithosphere is thin (high heat fluxes), strain is localized in numerous fault-like zones, with less absolute strain partitioned within each. After 1% extension, virtually all of the horizontal strain has been accommodated in just 2-3 zones (per 80 km) in a simulation with F=50 mW m^{-2}, whereas horizontal strain is accommodated in numerous smaller-scale regions in a simulation with F=100 mW m^{-2}. Additionally, in the low heat flux case the majority of the horizontal strain is accommodated diffusively within the groove trough itself, whereas in the high heat flux case the the near-surface strain is accommodated by down-dropping within the graben-like troughs.

At strains larger than about 1%, amplitude growth occurs roughly exponentially and at a similar rate for each heat flux. The growth curves therefore generally remain parallel to one another in Fig. 5B. Primarily because of the rapid early topography growth in the lower heat flux simulations, these low-heat-flux simulations still exhibit larger amplitudes by ∼6% strain (460 m vs. 200 m maximum amplitude for simulations with F=50 mW m^{-2} and 100 mW m^{-2}, respectively). As illustrated in Fig. 6, the surface deformation largely remains periodic up to 6% extension. At extensions larger than 7%, however, simulations transition from an extensional mode in which strain is broadly-distributed in periodic structures (wide rifting) to one in which strain increasingly becomes localized within a single necked region (narrow rifting). This phenomena is clearly illustrated in Fig. 6. At large strain in each simulation (F of 50, 75, 100, and 150 mW m^{-2}) the amplitude of a single groove trough grows at the expense of the rest of the topography. The localization of strain within a single trough occurs at lower extensions for high heat fluxes than for low heat fluxes. Thus for F=150 mW m^{-2} narrow rifting begins at just 7% extension, whereas for F=50 mW m^{-2} narrow rifting begins at 10% extension. Figure 5B shows the same transition to narrow rifting for the F=150 mW m^{-2} and 125 mW m^{-2} simulations, which undergo a rapid increase in amplitude growth at strains above 7%.

Care must be used when interpreting the transition to narrow rifting. Our simulations do not include thermal conduction, so warm ice from depth is upwelled passively into the necked regions but does not cool conductively. For our high heat flux simulations the lithosphere thins to just 1–2 km within the narrow rift zone. The thermal diffusion timescale ($\tau = h^2/\kappa$, where h and κ are the lithospheric thickness and thermal diffusion, respectively) for a 1 km thick lithosphere is of the same order as our simulation timescale ($\sim 10^{12}$ sec). Thus in these simulations the upwelling ice should cool, decrease in viscosity, act to stabilize the flow at depth, and limit additional thinning to some degree. Our numerical results, which implicity assume that thermal diffusion timescales are longer than simulation timescales, are therefore not accurate toward the end of these particular simulations. This caution does not imply, however, that the transition to narrow rifting is purely a numerical artifact. In the high heat fluxes cases the lithosphere is relatively thick (3 km) when the transition to narrow rifting begins and in the 50 mW m^{-2} and 75 mW m^{-2} the lithosphere is 7 km and 6 km thick, respectively. In these cases our assumptions regarding the thermal diffusion timescale is clearly not violated. Nor are the necked regions purely edge effects, for example.

Conditions that lead to either "wide" rifting or "narrow" rifting have been investigated in terrestrial settings (e.g., Buck, 1991; Precigout and Gueydan, 2009; Lu et al., 2011) and for icy satellites (Nimmo, 2004, based on Buck, 1991). These investigations suggest that the mode of extension results from the change in the force required to continue lithospheric extension once some finite extension has occurred. If the force required to continue extension increases the rift widens, and if the force decreases the rift remains localized (Buck, 1991). In an icy satellite the forces in play include the integrated strength of the lithosphere, thermal buoyancy (due to warm ice at depth), isostatic buoyancy if a subsurface ocean is present (Nimmo, 2004), and possibly other effects such as shear heating. Although the postulated model above cannot be directly applied to our simulations, they provide a useful conceptual framework for interpreting our results. Our simple models include neither thermal buoyancy nor isostasy (we use a constant density, and implicity assume a thick ice shell). Thus only the lithospheric strength and topographic stresses control the mode of extension. Initially, the lithosphere is nearly uniform and discrete fault-zones are broadly distributed. As extension continues the preferential localization of strain within a few groove troughs acts to effectively weaken the lithosphere in those locations, but at the same time, compressional stresses from the intervening topographic swells oppose this lithospheric weakening. Eventually a single fault zone becomes weak enough (through lithospheric thinning) that most or all of the deformation is accommodated within that zone and the transition to narrow rifting begins.

The question naturally arises whether localized narrow rifting is actually observed within swaths of groove terrain. Our ability to detect such narrow rifts is somewhat hampered by limited high resolution imaging and topography data. The types of localized rifting observed in our simulations would produce a single rift a factor of two or more deeper than the surrounding groove amplitudes; however, such a feature may not stand out in current imaging data (e.g., at high solar incidence). Where we do have topography (e.g., Fig. 2) few obvious candidates for narrow rifting are observed within broader groove swaths. However, especially deep bounding troughs *are* frequently observed at the margins of grooved terrain swaths (Shoemaker et al., 1982; Pappalardo et al., 1998; Prockter et al., 2000; Pappalardo et al., 2004). These troughs are morphologically consistent with our simulations when the narrow rifting occurs at the edge of the domain (e.g., the 150 mW m^{-2} case in Fig. 6).

Because the transition to narrow rifting occurs more readily at higher heat fluxes and larger strains, the absence of obvious narrow rifts within grooved terrain on Ganymede may indicate that both the heat fluxes and amount of extension were relatively modest (in general we don't *need* more than 10% extension if cold surface temperature are assumed). Alternatively, narrow rifts on Ganymede may have manifested as discrete regions of shell ice separation and translation, as Nimmo (2004) interprets Europa's tectonics. Hence the formation of Arbela-Sulcus-like bands on Ganymede (Head et al., 2002) may be consistent with higher heat flows and larger strains.

3.3 The effect of dilation angle

As discussed in Section 2, the dilation angle of ice is only weakly experimentally constrained, although we certainly expect it to be limited along active faults or shear zones. Figure 7 illustrates the effect of dilation angle on amplitude growth in our simulations. We find that, for dilation angles of 14° or less, our qualitative results are independent of the exact value of dilation used. A simulation identical to the simulation shown in Fig. 3A but with

with $\psi = 7°$, results in a maximum amplitude of 550 m, and an average amplitude of 280 m. The modest increase in maximum amplitude at $\psi = 7°$ relative to $\psi = 4°$ results from an earlier transition to narrow rifting in the $\psi = 7°$ case. The same phenomena is observed in the $\psi = 14°$ simulation, though its notable that the reduced degree of localization results in modestly smaller groove amplitudes at strains less than 8%. These results contrast strongly with those using associated plasticity ($\psi = 30°$), which result in a maximum amplitude of just 60 m after 10% strain.

3.4 Comparison to Ganymede's grooves

Figure 8 compares the deformation resulting from our simulations with large-amplitude groove topography derived from *Voyager* images of Bubastis Sulci in Ganymede's southern polar region. Our simulations of groove formation compare favorably with the general large-scale morphology of the grooved terrain. Both show large-amplitude, strongly-periodic ridge and trough structures of similar wavelength, topographic amplitude, and slope. The maximum and average amplitude of the measured grooves in Fig. 8B are ∼600 m and 330 m, respectively. These grooves are some of the largest groove structures on Ganymede, where measured groove amplitudes are generally less than 500 m, though some can reach as high as 700 m (Pappalardo et al., 2004). The real and simulated topography have similar maximum slopes (15°), though the average slopes are higher in the grooved terrain (i.e., high slopes occur more frequently), giving the profile a somewhat more jagged appearance in some regions (e.g., the sharp peaks at 70 and 95 km).

Whereas both the maximum and average amplitude of the grooves are roughly 33% larger than the simulated grooves after 10% extension (14% in the T_s=100 K case), the deformation amplitudes can be matched simply by permitting modestly larger total strain magnitudes (11-12% for the T_s=70 K simulation). Such strains are likely reasonable for the production of Ganymede's largest amplitude grooves, as discussed below. Larger groove amplitudes are also achievable with lower heat fluxes, which, as described above (see Fig. 5B), result in larger topographic amplitudes; however, the wavelength of the grooves (∼7 km) is consistent with a heat flux near 100 mW m^{-2} as shown in Fig. 8. Alternatively, lower strain rates generally result in large growth rates (at least until very low strain rates are reached (Dombard and McKinnon, 2001)). For the present numerical models, decreasing the strain rate by an order of magnitude (to 10^{-14} s^{-1}) results in a modest (10%) increase in groove amplitudes at 2% extension.

The wavelength of the topography fundamentally depends on the thickness of the lithosphere (H). Semi-analytical models of periodic necking instabilities have found that the ratio λ/H, where λ is the dominant topographic wavelength, is generally 3–4 (Fletcher and Hallet, 1983; Dombard and McKinnon, 2001). In contrast, our simulations consistently result in $\lambda/H \approx 2$. For example, after 5% extension, the lithospheric thickness in the simulation shown in Fig. 3A is 4.2 km and the wavelength is 7.2 km, yielding $\lambda/H = 1.7$ (we define the lithospheric thickness as the thickness of the layer in which plastic failure occurs). A similar simulation with F =25 mW m^{-2} has a lithospheric thickness of 14 km and wavelength of 30 km, yielding $\lambda/H = 2.1$. Our lower values of λ/H are generally consistent with our previous modeling, in which we found even lower values of $\lambda/H \approx 1 - 1.5$ (Bland and Showman, 2007). This result may suggest that the *effective* thickness of the lithosphere in our simulation is smaller than the apparent thickness, likely due to our use of a depth dependent yield strength (not considered in the analytical models). Notably, in simulations of lithospheric shortening in which we have removed the yield strength's depth dependence (i.e., conditions comparable to Dombard and McKinnon (2006)) we achieve λ/H values comparable to analytical values (Bland and McKinnon, 2012).

Our simulations indicate that the heat flux on Ganymede during groove formation likely exceeded 50 mW m^{-2} at the time of groove formation — a heat flux that yields topographic wavelengths of 16–20 km assuming a strain rate of 10^{-13} s^{-1}. At these strain rates, producing groove wavelengths shorter than 5 km requires heat fluxes greater than 150 mW m^{-2}, a value that may exceed plausible heat fluxes even during passage through proposed paleo-resonances (Bland et al., 2009). It is perhaps more likely that short-wavelength grooves (and perhaps all grooves) formed at lower strain rates, which result in modestly thinner lithospheres. Even in that case, however, forming grooves with λ ~5–10 km requires heat fluxes of 75 mW m^{-2} to 100 mW m^{-2}. Our inferred heat fluxes are consistent with previous analytical results (Dombard and McKinnon, 2001).

Figure 9A shows a zoomed-in portion of our finite element mesh for the nominal simulation with T_s=70 K described above. The figure isolates a single trough for detailed comparison with groove structures inferred from observations. Figure 9B shows a simple sketch of the key features of the simulated lithosphere. As described above, the subsurface deformation is distinctly graben-like, with large antithetically dipping fault-like zones bounding the trough. At high resolution it becomes clear that plastic failure (i.e., strain) is localized in individual linear structures (a single element in width) that intersect at depth to form a broader zone of plastic deformation. Despite symmetric topography, the structure is modestly asymmetric, with more numerous fault-like structures on the left hand side of the graben.

The structures suggested by our simulation contrast with the canonical view of ridge-like groove formation, which suggests that large-scale grooves (and their accompanying small-scale features) form via tilt-block faulting, in which all of the faults dip in the same direction (e.g., Collins et al., 1998; Pappalardo et al., 1998) (Fig. 9C). Whereas tilt-block-like structures are observed adjacent to larger bounding fault-like zones, in no cases do our simulations exclusively form parallel, same-dip sense, tilt-block zones of fault-like deformation. Instead the structures produced by our simulations (Fig. 9D) are more reminiscent of the structures inferred for the graben-like "lineated" grooved terrain described above (Pappalardo et al., 1998). In truth, the dominance of listric, tilt block, or antithetic faulting in grooved terrain is not known. In our modeling, with its uniform material properties and symmetric pure shear boundary conditions, symmetric faulting is expected. On Earth, the prevalence of symmetric or asymmetric faulting in extension has been ascribed to, or modeled as being due to, among other things, isostatically-upwelling, hot mantle (Buck, 1991; Nagel and Buck, 2007), shear heating and shear band formation (Lu et al., 2011), or simply lateral variations (e.g., Corti et al., 2013) or classic, regional simple shear (Wernicke, 1985; Brun, 1999). Any of these (or similar) effects could be invoked for Ganymede, and we note that our previous grooved terrain models that incorporated strain weakening developed notable asymmetric faults geometries (Bland et al., 2010)

The surface morphology produced by our simulations is consistent with observations of ridge-like grooved terrain. We argue, however, that both the ridge-like grooves and the lineated-grooves of Pappalardo et al. (1998) can be formed by the same general graben-like structures (i.e., antithetically dipping faults) with differing degrees of localization on a single discrete fault (as also suggested by Bland et al. (2010)). In the case of lineated-grooves, most of the strain is partitioned onto a single set of antithetic faults, whereas in the case of ridge-like grooves strain is partitioned across a much broader set of antithetic faults. The strong periodicity observed both on Ganymede and in our simulations indicates that, in both cases, the large-scale deformation is set by a necking-like instability. Groove formation involves a complex interplay between unstable extension, which concentrates stress and strain in the lithosphere, and the detailed mechanics of brittle failure and localization within the lithosphere.

3.5 The effect of surface temperature

Most of the simulations described above use a surface temperature of 70 K. On present day Ganymede, such a cold temperature is only relevant to the polar regions. It has been theoretically well established that surface temperature can play a prominent role in controlling tectonic deformation on icy satellites (e.g., Dombard and McKinnon, 2001, 2006; Bland and McKinnon, 2013). Temperatures on Ganymede range from 50 K (current polar) to nearly 120 K (current diurnally averaged equatorial; Dombard and McKinnon, 2001). Figure 10 shows the effect of surface temperature on maximum peak to trough groove amplitudes for our nominal simulation (F =100 mW m^{-2}) at 2%, 5%, and 10% extension. Groove amplitudes are strongly inhibited by warm surface temperatures, consistent with expectations from previous modeling (Dombard and McKinnon, 2001). For a surface temperature of 120 K, we find groove amplitudes reach only 50 m after 10% extension.

Dombard and McKinnon (2001) noted that, at the time that the grooved terrain formed ~2 Ga ago (Zahnle et al., 2003), surface temperatures were likely cooler than at present due to both an increased surface albedo (i.e., due to brighter, "cleaner" ice) and a fainter young Sun. They estimated equatorial temperatures of 100 K, as indicated in Fig. 10. At these temperatures maximum groove amplitudes reach just over 200 m after 10% extension, a factor of two or three lower than Ganymede's large amplitude grooves. The smaller amplitude growth rates can be compensated for, in principle, by increased extensional strain (>10%).

A modest increase in groove-amplitude growth rates at T_s =100 K can be achieved by decreasing the assumed heat flux. Because the surface temperature and heat flux combine to set the viscosity structure of the lithosphere, warmer surface temperatures yield thinner lithospheres and, for a given heat flux, push groove deformation to shorter wavelengths. For a heat flux of 100 mW m^{-2}, as shown in Fig. 10, the wavelength of deformation decreases from 7 km with T_s =70 K to 5 km with T_s =100 K. Because longer-wavelength deformation results in larger amplitudes (as discussed above), decreasing the heat flux and increasing the lithospheric thickness results in longer-wavelength, larger-amplitude grooves. Thus, at warmer surface temperatures, producing long-wavelength (7 km), large-amplitude topography requires lower heat fluxes than at colder surface temperatures, consistent with the effects of surface temperature on lithospheric shortening (Bland and McKinnon, 2013). We find, however, that the direct effect is small. The simulations shown in Fig. 3B with a surface temperature of T_s =100 K and heat fluxes of 75 mW m^{-2} results in grooves with an average wavelength of 7.6 km and a maximum amplitude of 215 m after 10% extension, an increase of only 25 m over the 100 mW m^{-2} case. Importantly, however, the lower heat flux also prevents a transition to narrow rifting at larger strains, and periodic structures reach an amplitude of ~410 m by 14% extension. Simulations with surface temperatures of 70 K and 100 K can therefore produce similar topography if the 100 K case experienced a lower heat flux and larger strains.

Our simulations would predict that, assuming similar distributions of strain and heat flux with latitude (not a good assumption if heating was due to tidal dissipation; Ojakangas and

Stevenson, 1989), both groove amplitudes and wavelengths should be larger in Ganymede's polar regions relative to the equatorial regions. No such obvious pattern has, to our knowledge, been noted. Although numerous, large-amplitude groove sets occur near Ganymede's south poles (e.g., Bubastis Sulci), large-amplitude grooves are also known in equatorial regions (e.g., amplitudes in Tiamat Sulcus reach 200-400 m). Strain magnitudes, strain rates, and heat fluxes, likely varied spatially during groove formation, so a survey of the global distribution of groove amplitudes and wavelengths, such as by a future mission to the Jupiter system, could be of great value in this regard.

4 Discussion

4.1 Implications for the global expansion of Ganymede

The simulations described above generate groove-like topography with extensional strains of just ∼10%. The smaller regional strains implied by our model is more consistent with the inference of low global strains on Ganymede (McKinnon, 1981) and may fall within the range of global expansion plausible from models of ice shell melting (Showman et al., 1997; Bland et al., 2009). As discussed above, localized strains on Ganymede may be as large as 100% in some localities; however, the regional strain associated with formation of much of the grooved terrain *must* be much lower in general. If large amplitude grooves can form in 10% extension (instead of 100%), the formation of Bubastis Sulcus (as described above) requires only a 60 km increase in Ganymede's circumference (only a 0.7% increase in surface area). Current global strain inventories (e.g., Collins, 2009) are somewhat hampered by the lack of data at sufficient resolution. Additionally, any such inventory must necessarily make assumptions regarding the structural geometry of the groove terrain, which as our simulations demonstrate, is far from certain. As above, both the imaging data, and subsurface structure, may eventually be provided by camera and radar systems on a future Ganymede mission, such as ESA's planned Jupiter Icy Moons Explorer.

Although our simulations do not require large strains to produce groove-like morphologies, neither do they prohibit the existence of large local strains. Instead, they provide a natural mechanism for simultaneous large, local extension and much smaller regional-scale extension. Compelling evidence for large local strains exists (Pappalardo and Collins, 2005). Nevertheless, much of this evidence comes from very localized sources: the scale of single 20-30 km craters. The tectonic deformation that disrupts these craters is generally only 10-20 km wide. These relatively narrow structures are of similar scale to one or two "*Voyager*-scale" groove troughs (e.g., Fig. 9). It is precisely within these small regions that extensional strain is localized in our simulations, with substantially higher strain magnitudes than the overall background extension imposed on the lithosphere. Figure 11 shows the distribution of total horizontal strain (i.e., extension) in our simulations. Whereas the imposed regional strain is only 10%, maximum extensional strains in the lithosphere can exceed 60% and strain at the surface reaches 35%. These larger strain values are more consistent with the measurements of strain across extended craters and the inference of extension required to produce large-amplitude grooves. We therefore argue that disrupted craters that indicate large strains are not necessarily representative of regional strains themselves but simply act as the locus (i.e., a local neck) of regional extension with smaller overall magnitude.

Our new simulation help establish a more consistent picture of Ganymede's strain history on local, regional, and global scales. Local strains (on the scale of a crater or single groove trough) can be exceedingly large (100%), while regional strains (on the scale of of wide groove swath) remain modest (10%), and global strains remain within the bounds set by calculations of satellite differentiation or melting. Ganymede's strain history therefore is brought closer into a balance, wherein the strain we infer from observations matches theoretical constraints. However, such a balance only holds if contraction (i.e., lithospheric shortening) has not occurred on Ganymede. To date no features due to lithospheric shortening have been identified on Ganymede. On neighboring Europa, several sets of subtle fold-like features have been observed in high-resolution images (Prockter and Pappalardo, 2000). Bland and McKinnon (2012, 2013) have recently shown that several percent lithospheric shortening can be accommodated by low-amplitude folding of ice lithospheres simply through lithospheric thickening without producing obvious (i.e., large amplitude) surface deformation. There is no reason to expect different tectonic behavior on Ganymede[2]. In fact, Ganymede's darker surface (i.e., warmer) might further inhibit the formation of obvious fold structures and permit the accommodation of several percent lithospheric shortening regionally. Regional or even global contraction (e.g., during slow cooling after resonance-induced melting) cannot be ruled out for Ganymede. If contraction has occurred then the regional strain associated with groove formation need not be precisely balanced by global expansion. In such a case the magnitude of global expansion could remain small while permitting large local and even regional strain, perhaps driven, in part, by mobile-lid convection (Hammond and Barr, 2013) or tidal walking (Tufts et al., 1997; Hoppa et al., 1999) rather than global expansion alone.

Acknowledgements

The authors are greatly indebted to Paul Schenk for the topography data used in Figs. 2 and 8. This work was supported by NASA Planetary Geology and Geophysics and Outer Planets Research Programs NNX11AP16G and NNX09AP32G.

References

Allison, M. L., Clifford, S. M., 1987. Ice-covered water volcanism on Ganymede. J. Geophys. Res. 92, 7865–7876.

Barr, A. C., McKinnon, W. B., 2007. Convection in ice I shells and mantles with self-consistent grain size. J. Geophys. Res. 112, E02012, doi:10.1029/2006JE002781.

Beaumont, C., Kamp, P. J. J., Hamilton, J., Fullsack, P., 1996. The continental collision zone, South Island, New Zealand: Comparison of geodynamical models and observations. J. Geophys. Res. 101, 3333–3360, doi:10.1029/95JB02401.

---

[2] Other mechanisms for accommodating shortening have been proposed for Europa as well (Kattenhorn and Hurford, 2009), and may also be applicable to Ganymede

Biot, M. A., 1961. Theory of folding of stratified viscoelastic media and its implications in tectonics and orogenesis. Geol. Soc. Am. Bull. 72, 1595–1620.

Bland, M. T., McKinnon, W. B., 2012. Forming Europa's folds: Strain requirements for the production of large-amplitude deformation. Icarus 221, 694–709, doi: 10.1016/j.icarus.2012.08.029.

Bland, M. T., McKinnon, W. B., 2013. Does folding accommodate Europa's contractional strain? The effect of surface temperature on fold formation in ice lithospheres. Geophys. Res. Lett. 40, 2534–2538, doi:10.1002/grl.50506.

Bland, M. T., McKinnon, W. B., Showman, A. P., 2010. The effects of strain localization on the formation of Ganymede's grooved terrain. Icarus 210, 396–410, doi:10.1016/j.icarus.2010.06.008.

Bland, M. T., Showman, A. P., 2007. The formation of Ganymede's grooved terrain: Numerical modeling of extensional necking instabilities. Icarus 189, 439–456, doi:10.1016/j.icarus.2007.01.012.

Bland, M. T., Showman, A. P., Tobie, G., 2009. The orbital-thermal evolution and global expansion of Ganymede. Icarus 200, 207–221, doi:10.1016/j.icarus.2008.11.016.

Brun, J.-P., 1999. Narrow rifts versus wide rifts: inferences for the mechanics of rifting from laboratory experiments. Philos. T. R. Soc. Lond. – A 357, 695, doi:10.1098/rsta.1999.0349.

Buck, W. R., Nov. 1991. Modes of continental lithospheric extension. J. Geophys. Res. 96, 20161–20178, doi:10.1029/91JB01485.

Buck, W. R., Lavier, L. L., Babeyko, A., 2003. A numerical model of lithospheric extension producing fault-bounded basins and ranges. Int. Geol. Rev. 18, 712–723.

Buck, W. R., Poliakov, A. N. B., 1998. Abyssal hills formed by stretching oceanic lithosphere. Nature 392, 272–275.

Collins, G. C., 2006. Global expansion of Ganymede derived from strain measurements in grooved terrain. Lunar Planet. Sci. XXXVII 37, 2077.

Collins, G. C., 2008. Driving mechanisms for grooved terrain formation on Ganymede: Comparison of theory to global groove database. Lunar Planet. Sci. XXXIX, Abs. 2254.

Collins, G. C., 2009. The origin of grooved terrain on Ganymede. European Planet. Sci. Cong. 4, #516.

Collins, G. C., Head, J. W., Pappalardo, R. T., 1998. The role of extensional instability in creating Ganymede grooved terrain: Insights from Galileo high-resolution stereo imaging. Geophys. Res. Lett. 25, 233–236, doi:10.1029/97GL03772.

Collins, G. C., McKinnon, W. B., Moore, J. M., Nimmo, F., Pappalardo, R. T., Prockter, L. M., Schenk, P. M., 2010. Tectonics of the outer planet satellites. In: Watters, T. R., Schultz, R. A. (Eds.), Planetary Tectonics. Cambridge University Press.

Corti, G., Iandelli, I., Cerca, M., 2013. Experimental modeling of rifting at craton margins. Geopsphere 9, 138–154.

Davis, R. O., Selvadurai, A. P. S., 2005. Plasticity and Geomechanics. Cambridge University Press, New York.

Delescluse, M., Montési, L. G. J., Chamot-Rooke, N., 2008. Fault reactivation and selective abandonment in the oceanic lithosphere. Geophys. Res. Lett. 35, doi:10.1029/2008GL035066.

Dombard, A. J., McKinnon, W. B., 1996. Formation of grooved terrain on Ganymede: Extensional instability mediated by cold, diffusional creep. Lunar Planet. Sci. Conf. XXVII, 317–318.

Dombard, A. J., McKinnon, W. B., 2001. Formation of grooved terrain on Ganymede: Extensional instability mediated by cold, superplastic creep. Icarus 154, 321–336, doi:10.1006/icar.2001.6728.

Dombard, A. J., McKinnon, W. B., 2006. Folding of Europa's icy lithosphere: an analysis of viscous-plastic buckling and subsequent topographic relaxation. J. Struct. Geo. 28, 2259–2269, doi:10.1016/j.jsg.2005.12.003.

Durham, W. B., Stern, L. A., 2001. Rheological properties of water ice: Applications to satellites of the outer planets. Ann. Rev. Earth Planet. Sci. 29, 295–330, doi:10.1146/annurev.earth.29.1.295.

Fink, J. H., Fletcher, R. C., 1981. Variations in thickness of Ganymede's lithosphere determined by spacings of lineations. Lunar Planet. Sci. XII, 277–278.

Fletcher, R. C., Hallet, B., 1983. Unstable extension of the lithosphere: A mechanical model for basin-and-range structure. J. Geophys. Res. 88, 7457–7466.

Gammon, P. H., Klefte, H., Clouter, M. J., 1983. Elastic constants of ice samples by brillouin spectroscopy. J. Phys. Chem. 87, 4025–4029.

Gerbault, M., Henrys, S., Davey, F., 2003. Numerical models of lithospheric deformation forming the Southern Alps of New Zealand. J. Geophys. Res. 108, 2341, doi:10.1029/2001JB001716.

Gessner, K., Wijns, C., Moresi, L., 2007. Significance of strain localization in the lower crust for structural evolution and thermal history of metamorphic core complexes. Tectonics 26, TC2012, doi:10.1029/2004TC001768.

Giese, B., Oberst, J., Roatsch, T., Neukum, G., Head, J. W., Pappalardo, R. T., 1998. The local topography of Uruk Sulcus and Galileo Regio obtained from stereo images. Icarus 135, 303–316, doi:10.1006/icar.1998.5967.

Goldsby, D. L., Kohlstedt, D. L., 1997. Flow of Ice I by Dislocation, Grain Boundary Sliding, and Diffusion Processes. Lunar Planet. Sci. XXVIII, 429–430.

Goldsby, D. L., Kohlstedt, D. L., 2001. Superplastic deformation of ice: Experimental observations. J. Geophys. Res. 106, 11017–11030, doi:10.1029/2000JB900336.

Golombek, M. P., Allison, M. L., 1981. Sequential development of grooved terrain and polygons on Ganymede. Geophys. Res. Lett. 8, 1139–1142.

Golombek, M. P., Banerdt, W. B., 1986. Early thermal profiles and lithospheric strength of Ganymede from extensional tectonic features. Icarus 68, 252–265, doi:10.1016/0019-1035(86)90022-9.

Greenberg, R., 1987. Galilean satellites: Evolutionary paths in deep resonance. Icarus 70, 334–347.

Grimm, R. E., Squyres, S. W., 1985. Spectral analysis of groove spacing on Ganymede. J. Geophys. Res. 90, 2013–2021.

Hammond, N. P., Barr, A. C., 2013. Formation of Ganymede's grooved terrain through convection-driven resurfacing. Icarus 227, 206–209, doi:10.1016/j.icarus.2013.08.024.

Head, J., Pappalardo, R., Collins, G., Belton, M. J. S., Giese, B., Wagner, R., Breneman, H., Spaun, N., Nixon, B., Neukum, G., Moore, J., 2002. Evidence for Europa-like tectonic resurfacing styles on Ganymede. Geophys. Res. Lett. 29 (24), 4–1, doi:10.1029/2002GL015961.

Head, J. W., Pappalardo, R. T., Collins, G., Greeley, R., 1997. Tectonic resurfacing on Ganymede and its role in the formation of grooved terrain. Lunar Planet. Sci. XXVIII, 535–536.

Herrick, D. L., Stevenson, D. J., 1990. Extensional and compressional instabilities in icy satellite lithospheres. Icarus 85, 191–204, doi:10.1016/0019-1035(90)90110-U.

Hoppa, G., Tufts, B. R., Greenberg, R., Geissler, P., 1999. Strike-Slip Faults on Europa: Global Shear Patterns Driven by Tidal Stress. Icarus 141, 287–298, doi:10.1006/icar.1999.6185.

Huismans, R. S., Beaumont, C., 2002. Asymmetric lithospheric extension: The role of frictional plastic strain softening inferred from numerical experiements. Geology 30, 211–214.

Iwashita, K., Oda, M., 1999. The mechanics of granular material: An introduction. A. A. Balkema, Rotterdam.

Kattenhorn, S. A., Hurford, T., 2009. Tectonics of Europa. In: Pappalardo, R. T., McKinnon, W. B., Khurana, K. K. (Eds.), Europa. University of Arizona Press, Tucson.

Lade, P. V., 2002. Characterization of the mechanical behavior of sea ice as a frictional material. J. Geophys. Res. 107, 2377, doi:10.1029/2001JB000497.

Lu, G., Kaus, B. J. P., Zhao, L., 2011. Thermal localization as a potential mechanism to rift cratons. PEPI 186, 125–137, doi:10.1016/j.pepi.2011.04.006.

Malhotra, R., 1991. Tidal origin of the Laplace resonance and the resurfacing of Ganymede. Icarus 94, 399–412.

McKinnon, W. B., 1981. Tectonic deformation of Galileo Regio and limits to the planetary expansion of Ganymede 12.

Melosh, H. J., Raefsky, A., 1980. The dynamical origin of subduction zone topography. Geophys. J. R. Astr. Soc. 60, 333–354.

Mueller, S., McKinnon, W. B., 1988. Three-layered models of Ganymede and Callisto: Compositions, structures, and aspects of evolution. Icarus 76, 437–464.

Nagel, T. J., Buck, W. R., 2007. Control of rheological stratification on rifting geometry: a symmetric model resolving the upper plate paradox. Int. J. Earth Sci. 96, 1047–1057, doi:10.1007/s00531-007-0195-x.

Nimmo, F., 2004. Dynamics of rifting and modes of extension on icy satellites. J. Geophys. Res. 109, E01003, doi:10.1029/2003JE002168.

Ojakangas, G. W., Stevenson, D. J., 1989. Thermal state of an ice shell on Europa. Icarus 81, 220–241, doi:10.1016/0019-1035(89)90052-3.

Owen, D. R. J., Hinton, E., 1980. Finite elements in plasticity: Theory and practice. Pineridge Press Limited, Swansea, UK.

Pappalardo, R. T., Collins, G. C., 2005. Strained craters on Ganymede. J. Struct. Geo. 27, 827–838.

Pappalardo, R. T., Collins, G. C., Head, J. W., Helfenstein, P., McCord, T. B., Moore, J. M., Prockter, L. M., Schenk, P. M., Spencer, J. R., 2004. Geology of Ganymede. In: Bagenall, F., Dowling, T., McKinnon, W. B. (Eds.), Jupiter - The Planet, Satellites and Magnetosphere. Cambridge University Press, Cambridge, UK, pp. 363–396.

Pappalardo, R. T., Head, J. W., Collins, G. C., Kirk, R. L., Neukum, G., Oberst, J., Giese, B., Greeley, R., Chapman, C. R., Helfenstein, P., Moore, J. M., McEwen, A., Tufts, B. R., Senske, D. A., Breneman, H. H., Klaasen, K., 1998. Grooved terrain on Ganymede: First results from Galileo high-resolution imaging. Icarus 135, 276–302, doi:10.1006/icar.1998.5966.

Parmentier, E. M., Squyres, S. W., Head, J. W., Allison, M. L., 1982. The tectonics of Ganymede. Nature 295, 290–293.

Patel, J. G., Pappalardo, R. T., Head, J. W., Collins, G. C., Hiesinger, H., Sun, J., 1999. Topographic wavelengths of Ganymede groove lanes from Fourier analysis of Galileo images. J. Geophys. Res. 104, 24057–24074, doi:10.1029/1998JE001021.

Patterson, G. W., Collins, G. C., Head, J. W., Pappalardo, R. T., Prockter, L. M., Lucchitta, B. K., Kay, J. P., 2010. Global geologic mapping of Ganymede. Icarus 207, 845–867, doi:10.1016/j.icarus.2009.11.035.

Peale, S. J., Lee, M. H., 2002. A primordial origin of the Laplace relation among the Galilean satellites. Science 298, 593–597.

Petrenko, V. F., Whitworth, R. W., 1999. Physics of Ice. Oxford University Press, Oxford.

Poliakov, A. N. B., Herrmann, H. J., 1994. Self-organized criticality of plastic shear bands in rocks. Geophys. Res. Lett. 21, 2143–2146, doi:10.1029/94GL02005.

Precigout, J., Gueydan, F., 2009. Mantle weakening and strain localization: Implications for the long-term strength of the continental lithosphere. Geology 37, 147–150, doi:10.1130/G25239A.1.

Pritchard, R. S., 1988. Mathematical characteristics of sea ice dynamic models. J. Geophys. Res. 93, 15609–15618.

Prockter, L. M., Figueredo, P. H., Pappalardo, R. T., Head, J. W., Collins, G. C., 2000. Geology and mapping of dark terrain on Ganymede and implications for grooved terrain formation. J. Geophys. Res. 105, 22519–22540, doi:10.1029/1999JE001179.

Prockter, L. M., Pappalardo, R. T., 2000. Folds on Europa: Implications for crustal cycling and accommodation of extension. Science 289, 941–944, doi:10.1126/science.289.5481.941.

Rudnicki, J. W., Rice, J. R., 1975. Conditions for the localization of deformation in pressure-sensative dilatant materials. J. Mech. Phys. Solids 23, 371–394.

Schenk, P. M., McKinnon, W. B., Gwynn, D., Moore, J. M., 2001. Flooding of Ganymede's bright terrain by low-viscosity water-ice lavas. Nature 410, 57–60.

Schmalholz, A. M., 2006. Scaled amplification equation: A key to the folding history of buckled viscous single-layers. Tectonophys. 419, 41–53.

Schmalholz, A. M., Podladchikov, Y. Y., 2001. Strain and competence contrast estimation from fold shape. Tectonophys. 340, 195–213.

Schulson, E. M., Duval, P., 2009. Creep and fracture of ice. Cambridge University Press, Cambridge.

Shoemaker, E. M., Lucchitta, B. K., Wilhelms, D. E., Plescia, J. B., Squyres, S. W., 1982. The geology of Ganymede. In: Morrison, D. (Ed.), Satellites of Jupiter. University of Arizona Press, pp. 435–520.

Showman, A. P., Stevenson, D. J., Malhotra, R., 1997. Coupled orbital and thermal evolution of Ganymede. Icarus 129, 367–383, doi:10.1006/icar.1997.5778.

Smith, R. B., 1975. Unified theory of the onset of folding, boudinage, and mullion structure. Geo. Soc. Am. Bull. 86, 1601–1609.

Smith, R. B., 1977. Formation of folds, boudinage, and mullion in non-Newtonian material. Geo. Soc. Am. Bull. 88, 312–320.

Squyres, S. W., 1980. Volume changes in Ganymede and Callisto and the origin of grooved terrain. Geophys. Res. Lett. 7, 593–596.

Squyres, S. W., 1981. The topography of Ganymede's grooved terrain. Icarus 46, 156–168, doi:10.1016/0019-1035(81)90204-9.

Squyres, S. W., 1982. The evolution of tectonic features on Ganymede. Icarus 52, 545–559, doi:10.1016/0019-1035(82)90014-8.

Tremblay, L.-B., Mysak, L. A., 1997. Modeling sea ice as a granular material, including the dilatancy effect. J. Phys. Oceanog. 27, 2342–2360, doi:10.1175/1520-0485(1997)027¡2342:MSIAAG¿2.0.CO;2.

Tufts, R., Greenberg, R., Geissler, P., Hoppa, G., Pappalardo, R., Sullivan, R., Galileo Imaging Team, 1997. Crustal displacement features on Europa. AAS Div. Planet. Sci. Conf. #29 29, 983.

Vermeer, P. A., de Borst, R., 1984. Non-associated plasticity for soils, concrete, and rocks. Heron 29, 1–64.

Wernicke, B., 1985. Uniform-sense normal simple shear of the continental lithosphere. Can. J. Earth Sci. 22, 108–125.

Wilchinsky, A. V., Feltham, D. L., 2011. Modeling Coulombic failure of sea ice with leads. J. Geophys. Res. 116, 8040, doi:10.1029/2011JC007071.

Yasufuku, N., Springman, S. M., Arensen, L. U., Ramholt, T., 2008. Stress-dilatancy behaviour of frozen sand in direct shear. In: Permafrost. Swets and Zeitlinger.

Yoder, C. F., 1979. How tidal heating on Io drives the galilean orbital resonance locks. Nature 279, 767–770.

Zahnle, K., Schenk, P., Levison, H. F., Dones, L., 2003. Cratering rates in the outer solar system. Icarus 163, 263–289, doi:10.1016/s0019-1035(03)00048-4.

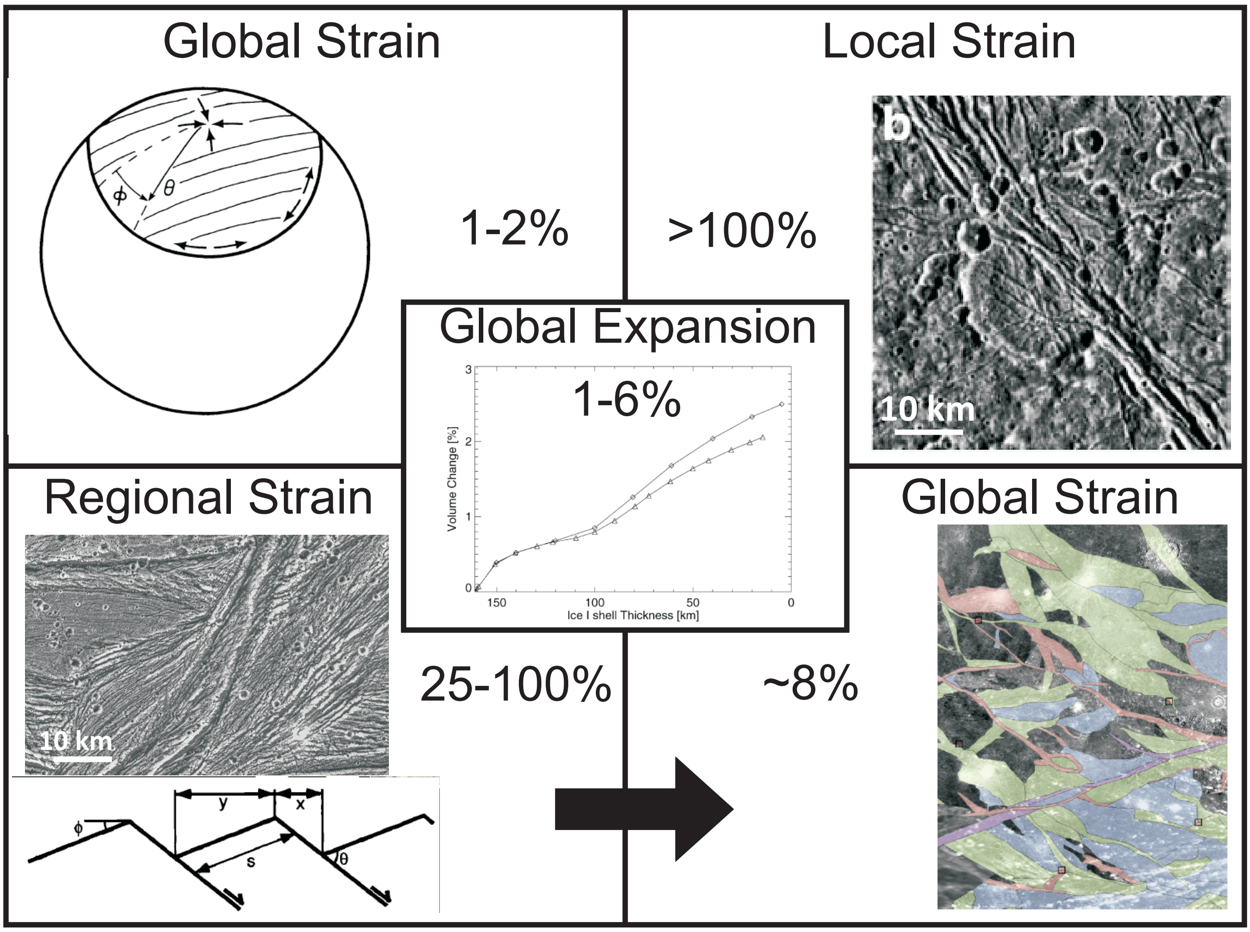

Figure 1: Summary of independent constraints on Ganymede's areal strain. **A.** The observation the Galileo Regio forms an intact spherical cap of dark terrain limits Ganymede's global expansion to $\leq$2% (McKinnon, 1981). **B.** Measurements of deformed craters indicate local strains can exceed $\sim$100% (Pappalardo and Collins, 2005). **C.** Structural reconstruction of grooved terrain suggest typical extensions of 25-100% for the formation of large amplitude grooves (Collins et al., 1998; Collins, 2006). **D.** Extrapolation of regional strain estimates from C suggest global surface strain of 8% (Collins, 2008). **E.** Theoretical calculations of the global strain available from differentiation or melting indicate maximum surface strains of 1-6%. Plot modified from (Bland et al., 2009).

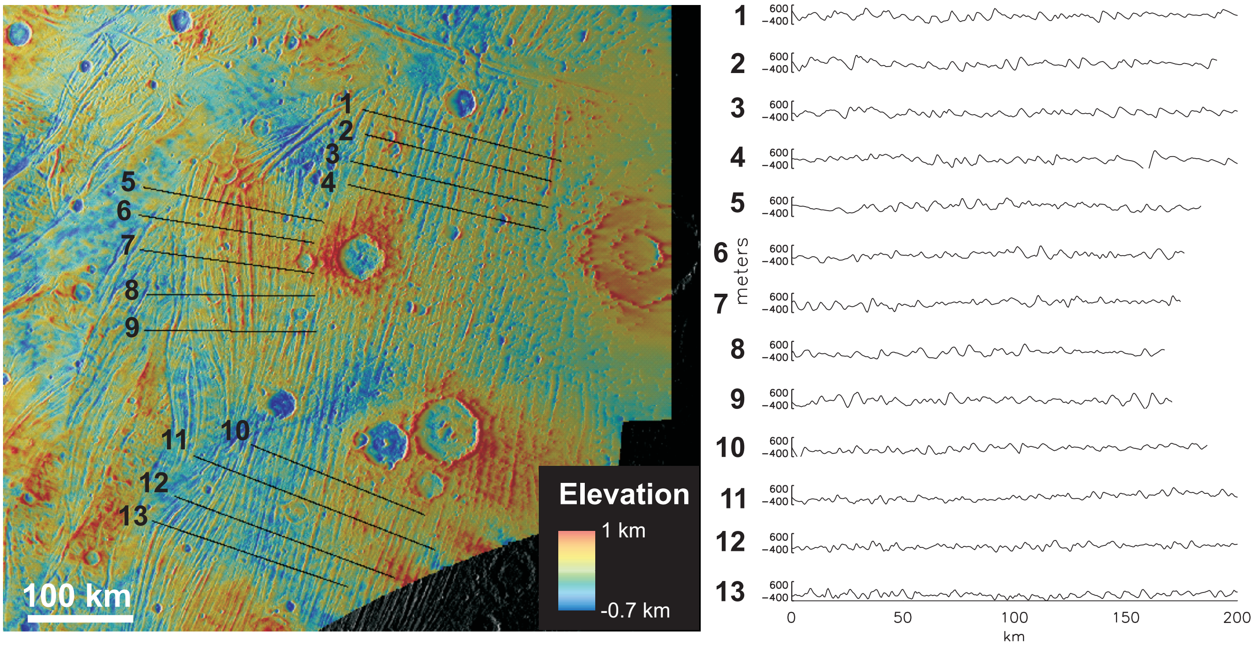

Figure 2: **A.** Combined stereo and photoclinometric topography overlayed on a *Voyager* image of the Bubastis Sulci region near Ganymede's south pole (pole located just off the bottom right corner of image). Topography and background image courtesy of Paul Schenk. **B.** Topographic profiles across Bubastis Sulci. Numbers correspond to the profile locations shown in panel A.

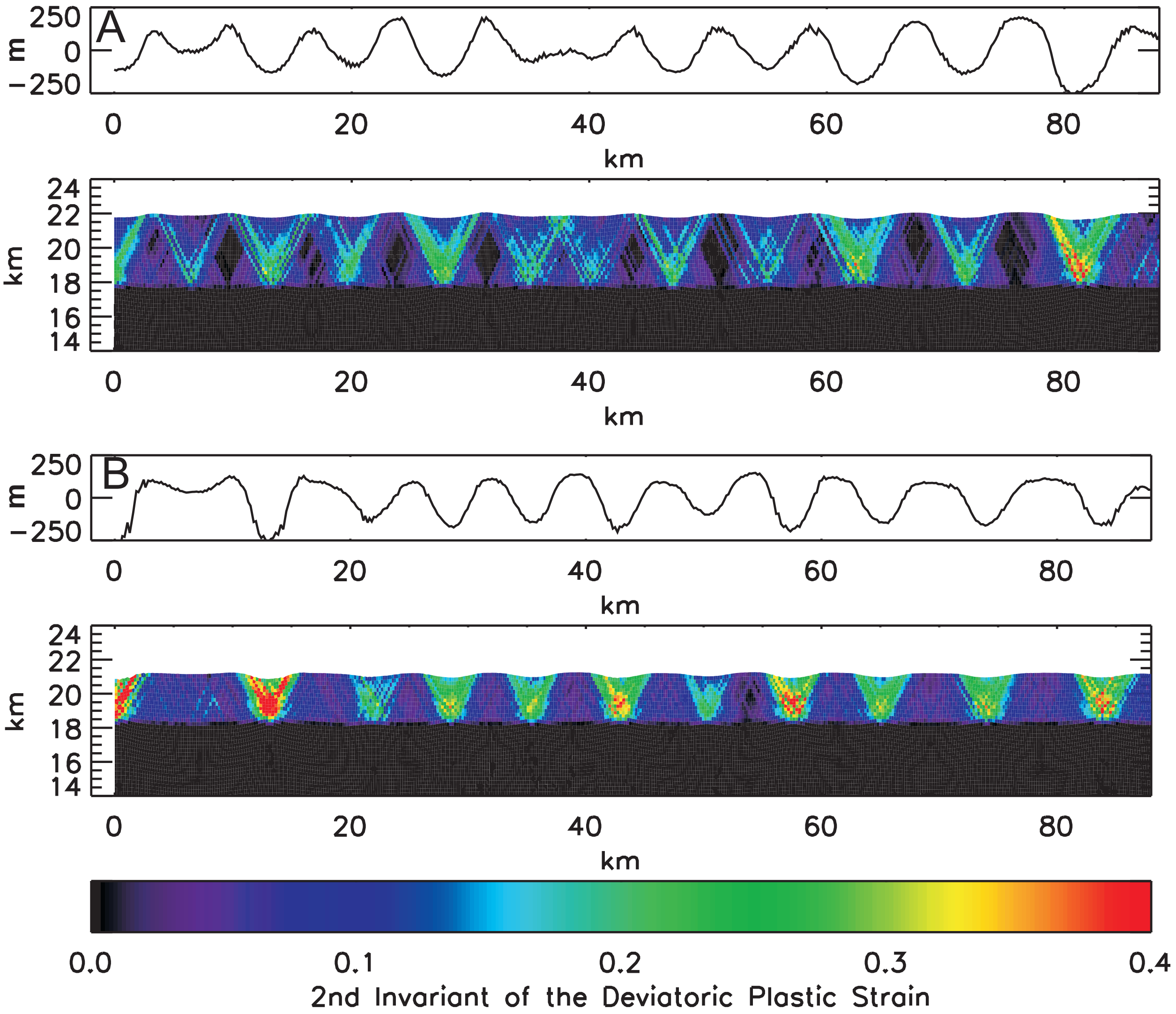

Figure 3: The trace of the relative surface deformation and the distribution of plastic strain (i.e., failure) for simulations with **A** T_s=70 K, F = 100 mW m^{-2}, $\dot{\varepsilon}$ = 10^{-13} s^{-1}, 10% extension, and **B** T_s=100 K, F = 75 mW m^{-2}, $\dot{\varepsilon}$ = 10^{-13} s^{-1}, 14% extension. Note that initial topography was random and small-scale (∼15 m maximum relief).

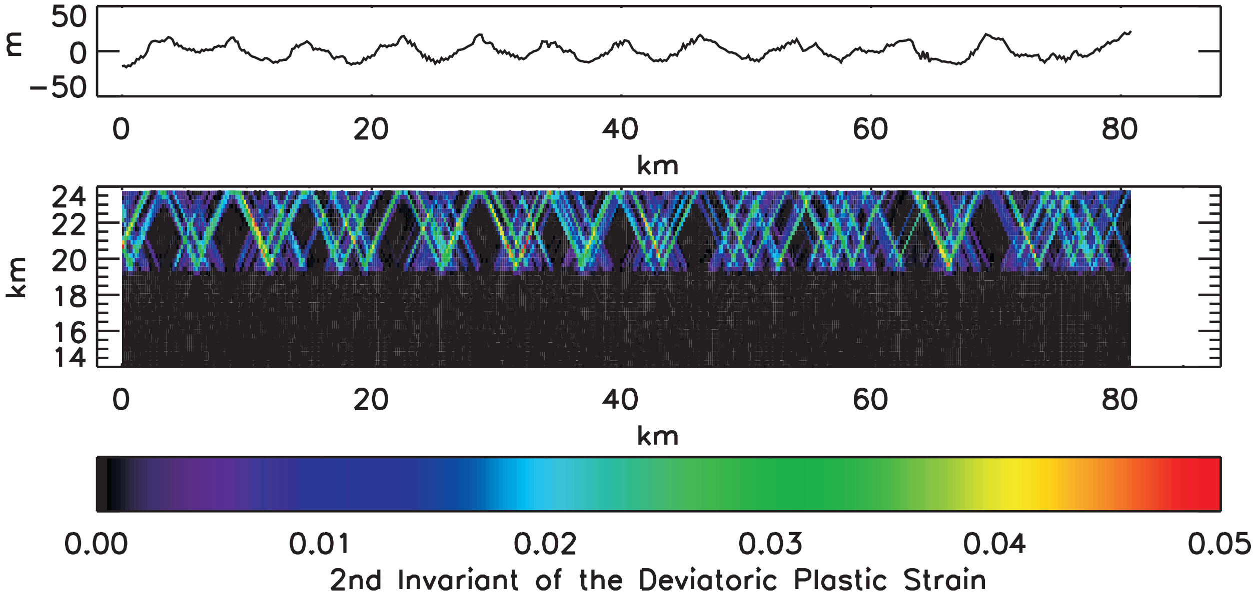

Figure 4: The same simulation as in Fig. 3A but after just 1% extension.

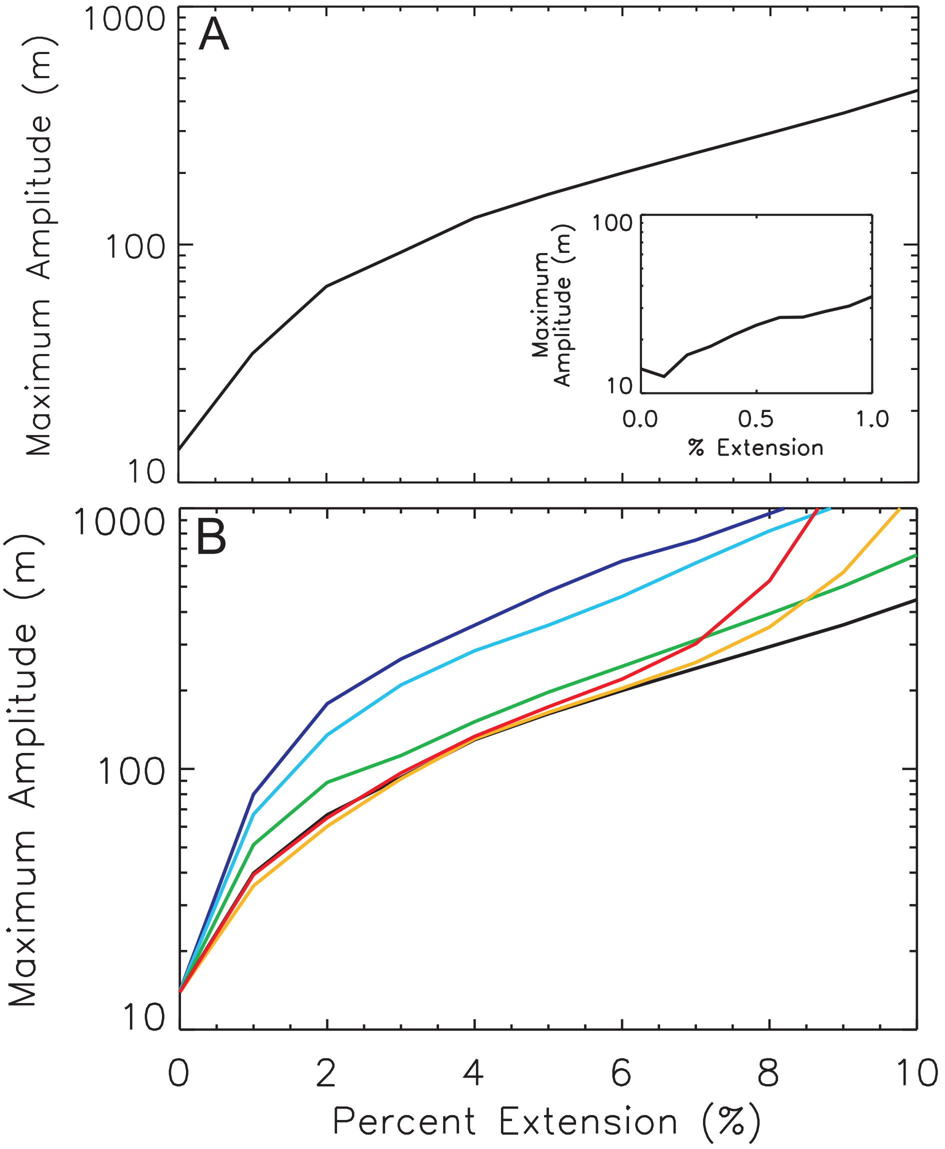

Figure 5: **A.** The maximum amplitude (peak to trough) as a function of extension for the simulation shown in Fig. 3A and 4 (100 mW m^{-2} and 10^{-13} s^{-1}). The inset shows topographic amplitudes below 1%. **B.** As in A but for simulations with a various heat fluxes (mW m^{-2}): 25 (dark blue), 50 (light blue), 75 (green), 100 (black), 125 (yellow), and 150 (red).

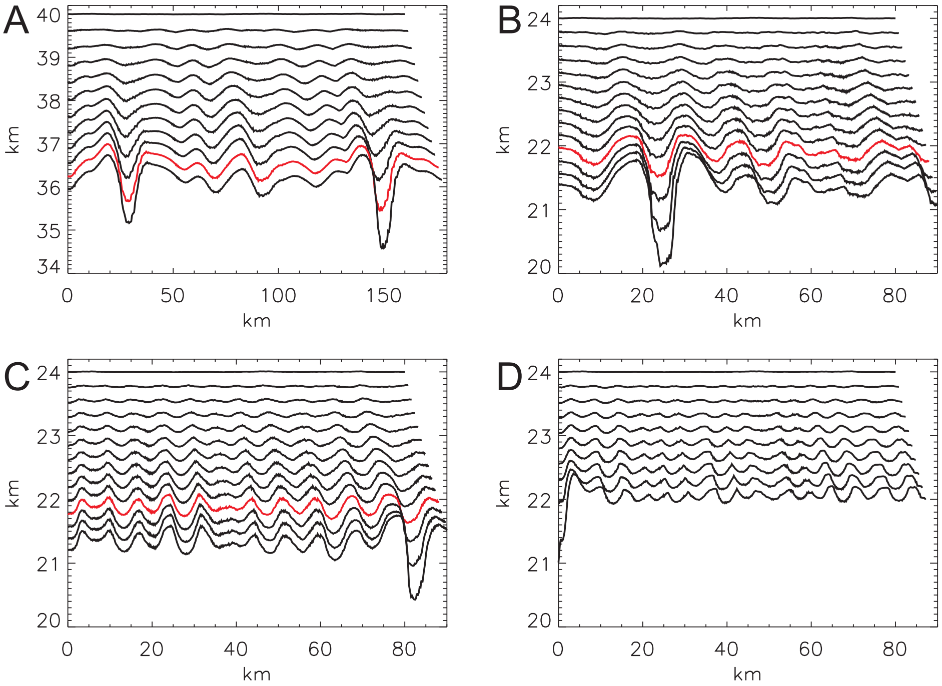

Figure 6: The trace of the surface deformation as a function of strain for heat fluxes of 50 mW m^{-2} (**A**), 75 mW m^{-2} (**B**), 100 mW m^{-2} (**C**), and 150 mW m^{-2} (**D**). In each panel the surface deformation is shown at increments of 1% extension beginning with the initial topography (e.g., 0%, 1%, 2% etc.). The red curve in each panel marks 10% extension. Note the difference in vertical and horizontal scale in A.

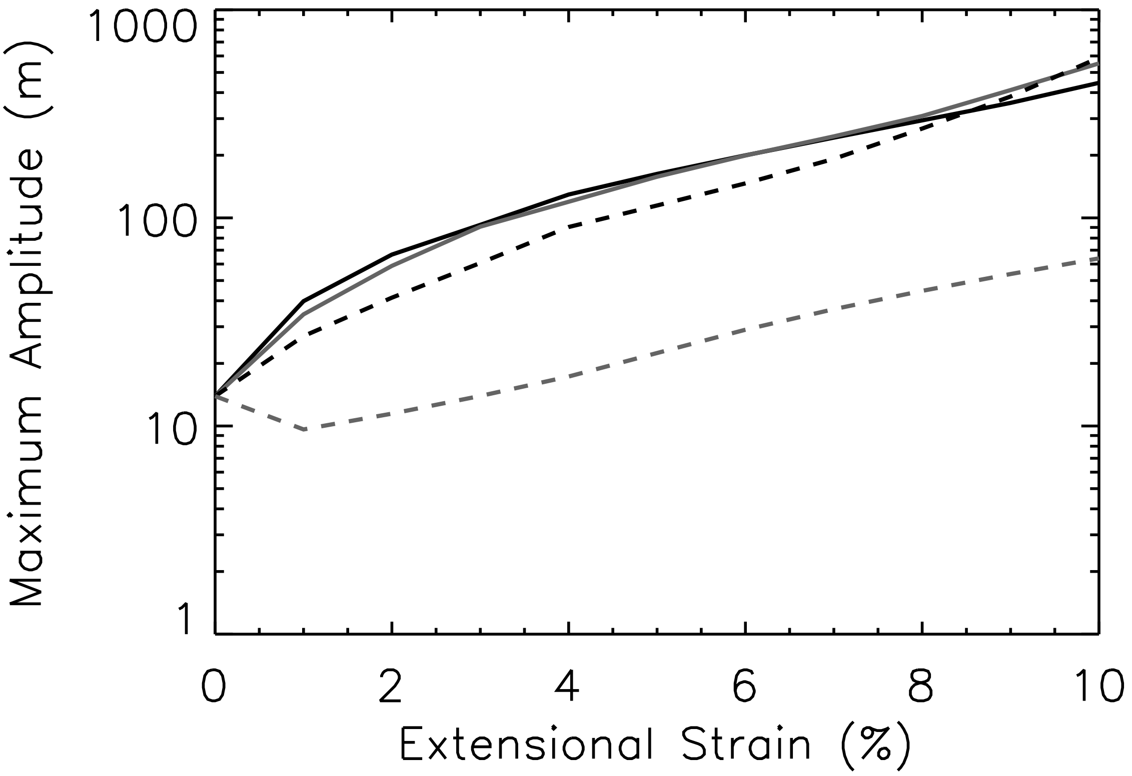

Figure 7: The maximum amplitude (peak to trough) as a function of extension for simulations with nominal conditions but dilation angles of 3.6° (nominal, black), 7.2° (grey), 14.3° (black dashed), and 30° (associative plasticity, grey dashed).

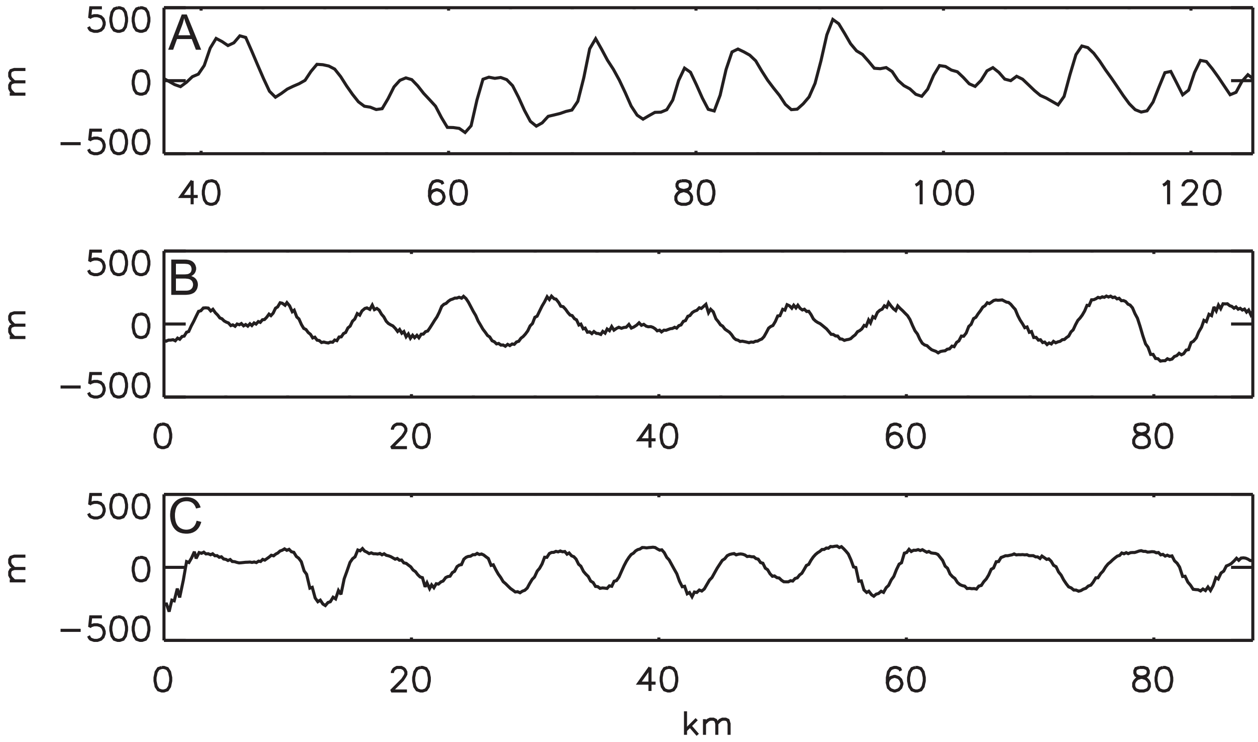

Figure 8: Comparison of groove topography (A) with the surface deformation produced by the simulations shown in Fig. 3 with a surface temperature of 70 K after 10% extension (B), and 100 K after 14% extension (C). The groove topography is a portion of profile 1 in Fig. 2. The simulations are as in Fig. 3.

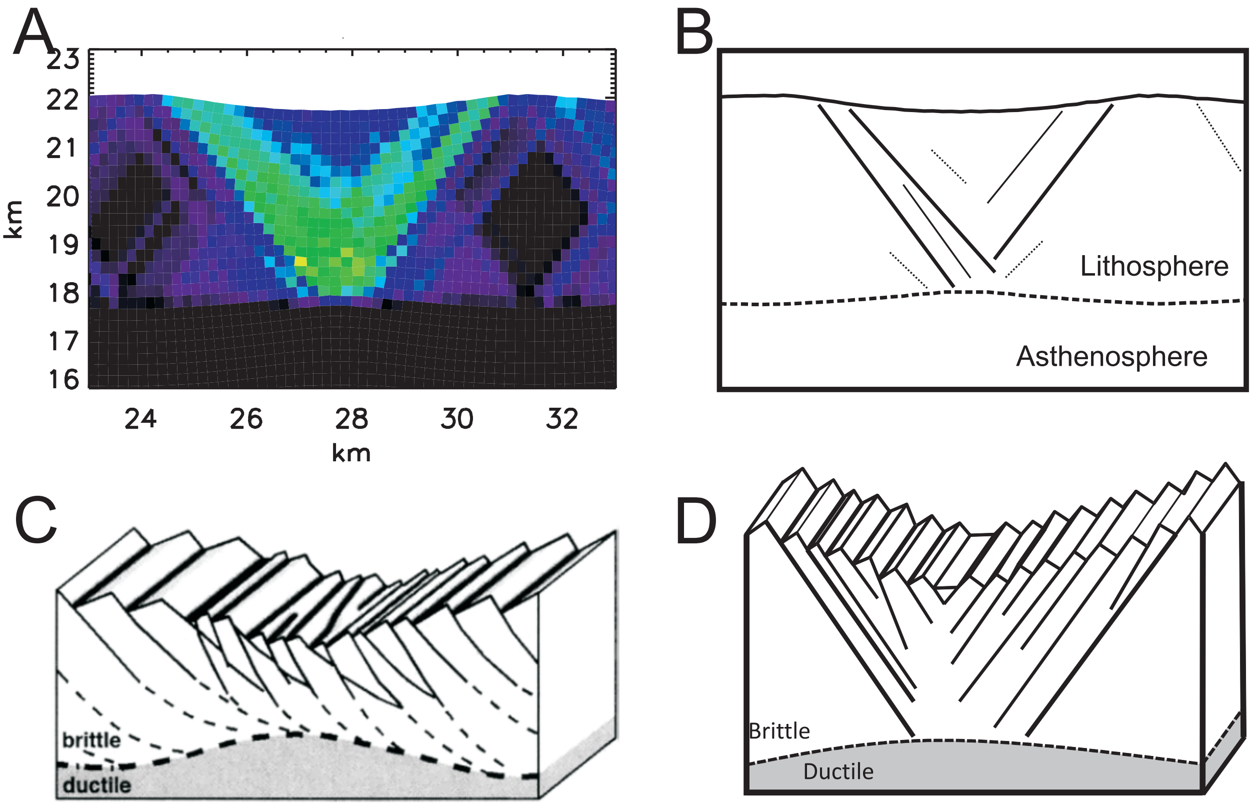

Figure 9: **A.** An enlarged portion of the finite element mesh shown in Fig. 3 illustrating the structural geometry produced by our simulated extension. **B.** A simple sketch map of the key geometrical components in A. **C.** The canonical block model of groove terrain geologic structures (modified from Collins et al., 1998) **D.** Block model consistent with the structures implied by the numerical simulations.

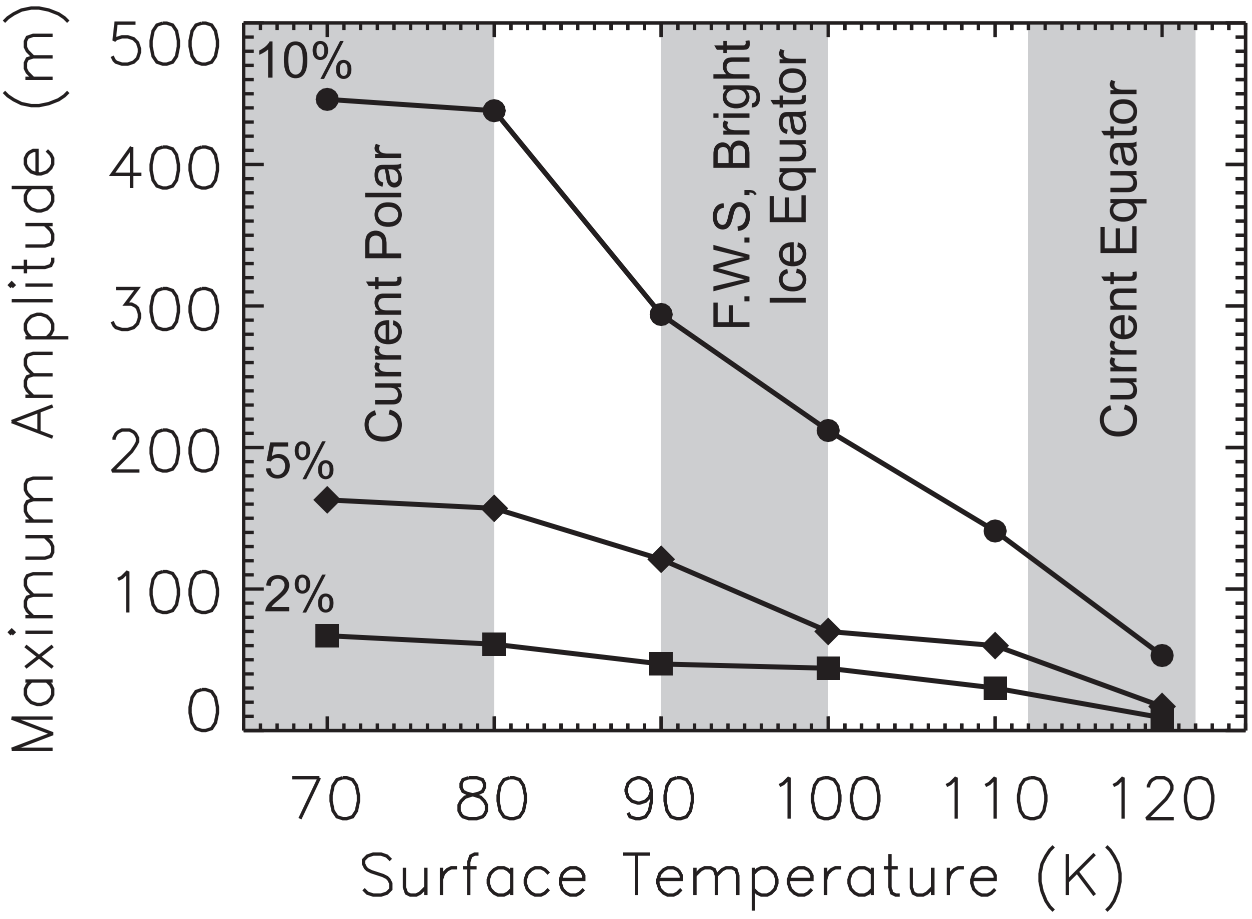

Figure 10: The effect of surface temperature on maximum groove amplitudes after 2% (squares), 5% (diamonds), and 10% (circles) extension. Shaded regions indicate typical temperatures at Ganymede's poles and equator, as well as the equatorial temperature at the time of groove formation when the Sun was fainter (F.Y.S) and if Ganymede's surface ice was photometrically "fresh" (Europa-like high albedo) (e.g. Dombard and McKinnon, 2001).

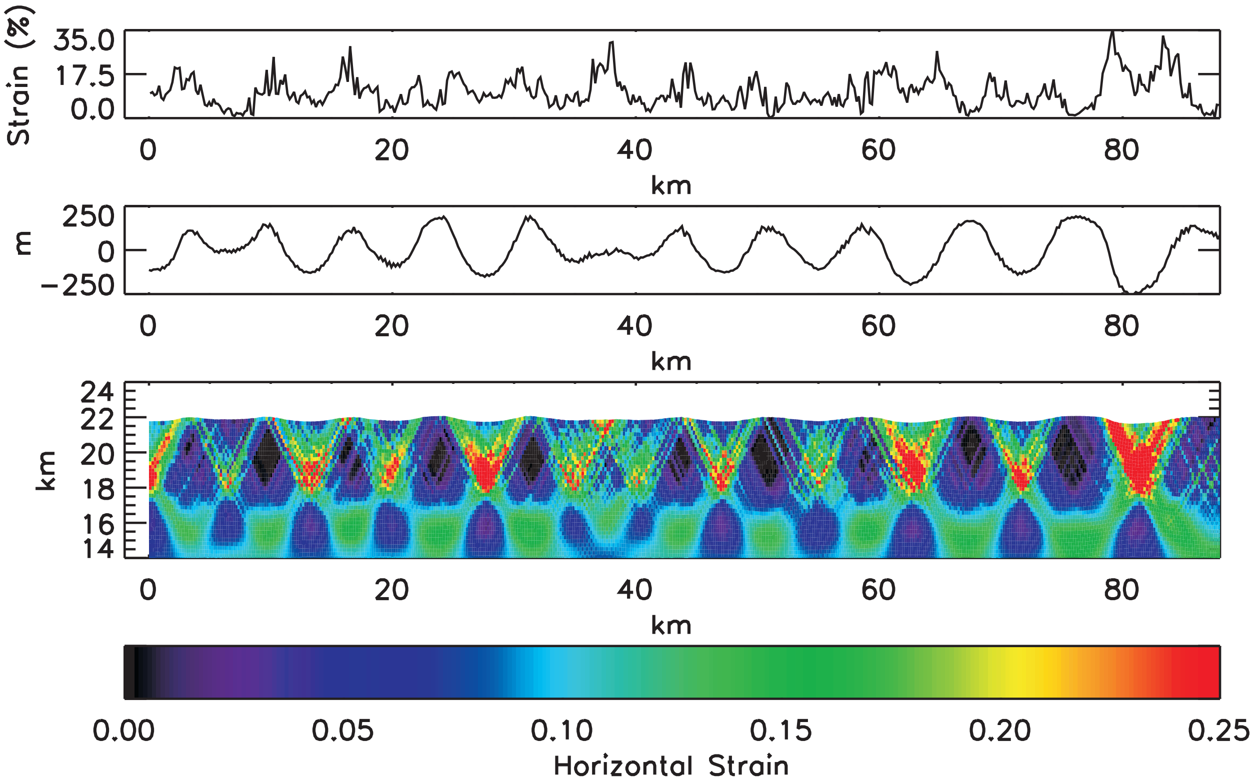

Figure 11: **Bottom** The distribution of horizontal strain within our nominal simulation after 10% extension. **Middle** the surface topography after 10% extension. **Top** The horizontal strain at the surface of the domain (top row of elements).